The Astrophysical Journal, 943:49 (15pp), 2023 January 20 https://doi.org/10.3847/1538-4357/acab04

The IGRINS YSO Survey. III. Stellar Parameters of Pre-main-sequence Stars in Ophiuchus and Upper Scorpius

Ricardo López-Valdivia[1,2], Gregory N. Mace[1], Eunkyu Han[1], Erica Sawczynec[1], Jesús Hernández[2], L. Prato[3], Christopher M. Johns-Krull[4], Heeyoung Oh[5], Jae-Joon Lee[5], Adam Kraus[1], Joe Llama[3], and Daniel T. Jaffe[1]
[1] The University of Texas at Austin, Department of Astronomy, 2515 Speedway, Stop C1400, Austin, TX 78712-1205, USA; rlopezv@astro.unam.mx
[2] Universidad Nacional Autónoma de México, Instituto de Astronomía, AP 106, Ensenada 22800, BC, México
[3] Lowell Observatory, 1400 W. Mars Hill Road, Flagstaff. AZ 86001, USA
[4] Physics & Astronomy Department, Rice University, 6100 Main Street, Houston, TX 77005, USA
[5] Korea Astronomy and Space Science Institute, 776 Daedeok-daero, Yuseong-gu, Daejeon 34055, Republic of Korea
Received 2022 September 2; revised 2022 December 8; accepted 2022 December 9; published 2023 January 24

Abstract

We used the Immersion GRating Infrared Spectrometer (IGRINS) to determine fundamental parameters for 61 K- and M-type young stellar objects (YSOs) located in the Ophiuchus and Upper Scorpius star-forming regions. We employed synthetic spectra and a Markov chain Monte Carlo approach to fit specific *K*-band spectral regions and determine the photospheric temperature (T), surface gravity ($\log g$), magnetic field strength (B), projected rotational velocity ($v \sin i$), and *K*-band veiling (r_K). We determined B for ∼46% of our sample. Stellar parameters were compared to the results from Taurus-Auriga and the TW Hydrae association presented in Paper I of this series. We classified all the YSOs in the IGRINS survey with infrared spectral indices from Two Micron All Sky Survey and Wide-field Infrared Survey Explorer photometry between 2 and 24 μm. We found that Class II YSOs typically have lower $\log g$ and $v \sin i$, similar B, and higher *K*-band veiling than their Class III counterparts. Additionally, we determined the stellar parameters for a sample of K and M field stars also observed with IGRINS. We have identified intrinsic similarities and differences at different evolutionary stages with our homogeneous determination of stellar parameters in the IGRINS YSO survey. Considering $\log g$ as a proxy for age, we found that the Ophiuchus and Taurus samples have a similar age. We also find that Upper Scorpius and TWA YSOs have similar ages, and are more evolved than Ophiuchus/Taurus YSOs.

Unified Astronomy Thesaurus concepts: Fundamental parameters of stars (555); Infrared sources (793); Pre-main sequence stars (1290); High resolution spectroscopy (2096)

Supporting material: machine-readable tables

1. Introduction

Young stellar objects (YSOs) are stars at an early stage of evolution and their properties have a dominant impact on the environments of planet development. Stellar parameters like temperature (T) and surface gravity ($\log g$) permit comparisons with evolutionary models (Baraffe et al. 2015; Simon et al. 2019). With these fundamental parameters, the differences between models and observations for stars with masses $<1.5\ M_{\odot}$ and age <10 Myr (e.g., Simon et al. 2013) can be better understood. The accurate and precise determination of YSO parameters is limited by the impacts of interstellar reddening, continuum veiling, and magnetic fields. These processes, if not considered, can result in inaccurate YSO parameters and thus lead to wrong conclusions about star formation and evolution.

For example, the veiling is a nonstellar continuum emission that reduces the depth of the photospheric lines in YSO spectra (Joy 1949). Such reduction of the line depth could lead to erroneous T or $\log g$ values as these parameters have similar effects on certain atomic lines. On the other hand, the presence of strong magnetic fields (B) changes the absorption line profiles through Zeeman broadening (e.g., Johns-Krull et al. 1999; Yang et al. 2005; Lavail et al. 2017; Sokal et al. 2018; Lavail et al. 2019; Sokal et al. 2020).

The Immersion GRating INfrared Spectrometer (IGRINS; Yuk et al. 2010; Park et al. 2014; Mace et al. 2016) was designed to minimize the problems associated with determining YSO parameters. IGRINS employs a silicon immersion grating as the primary disperser (Jaffe et al. 1998; Gully-Santiago et al. 2010; Wang et al. 2010) and volume phase holographic gratings to cross disperse the *H*- and *K*-band echellograms onto Teledyne Hawaii-2RG arrays. This setup provides a compact design with high sensitivity and a significant single-exposure spectral grasp at a spectral resolution of $R \sim 45{,}000$ (Yuk et al. 2010; Park et al. 2014). IGRINS has a fixed spectral format and no moving optics, so the science products are consistent over time baselines of several years. IGRINS has increased its scientific value by traveling among the McDonald Observatory, the Lowell Discovery Telescope (LDT), and the Gemini South telescope (Mace et al. 2018).

The IGRINS YSO survey is uniquely suited to determining physical parameters because (i) the simultaneous coverage of the *H* and *K* bands (1.45–2.5 μm) of IGRINS includes separable photospheric and disk contributions to the YSO spectrum. (ii) The fixed spectral format of IGRINS provides similar spectral products for each object at each epoch. (iii) Multiple-epoch observations can provide a means to characterize or average over variability. (iv) The velocity resolution of $\sim 7\ \mathrm{km\ s^{-1}}$ ($R \sim 45{,}000$) is smaller than the typical young star rotational velocity and can resolve magnetic fields $\gtrsim 1$ kG.

In López-Valdivia et al. (2021, hereafter Paper I), we presented the first results of the IGRINS YSO survey. This first study consisted of the determination of photospheric temperature (T), surface gravity ($\log g$), magnetic field (B), projected rotational velocity ($v \sin i$), and the K-band veiling (r_K) for 110 YSOs located in the Taurus-Auriga star-forming region and 19 young stars in the TW Hydrae association (TWA). The IGRINS YSO survey analysis continued with the determination of low-resolution veiling spectra for 144 Taurus-Auriga members in Kidder et al. (2021, hereafter Paper II). In this paper, the third of the series, we extend our analysis to K- and M-type YSOs in the Ophiuchus and Upper Scorpius star-forming regions (Elias 1978; Lada & Wilking 1984; Wilking et al. 1989). Combining the results of Paper I with those obtained here improved our understanding of YSO stellar parameters as a function of age.

2. Observations and Sample

Among the IGRINS YSO survey, we included bright objects ($K < 11$ mag) with spectral types between K0 and M5 (Wilking et al. 2005; Torres et al. 2006; Ricci et al. 2010; Esplin & Luhman 2020; Luhman & Esplin 2020), which were classified as members of Ophiuchus and Upper Scorpius by Hsieh & Lai (2013), Rebull et al. (2018), and Esplin & Luhman (2020).

We observed our sample with IGRINS at the McDonald Observatory 2.7 m telescope, the LDT, and the Gemini South Telescope between 2014 and 2019. We followed the observing and data reduction methods as outlined in Paper I. In brief, we observed the YSOs and A0V telluric standards[6] by nodding the stars along the slit in patterns made up of AB or BA pairs, where A and B are two different positions on the slit. We aimed to obtain a minimum signal-to-noise ratio (S/N) of 70 in the K band by adjusting the total exposure time based on the IGRINS exposure time calculator.[7] An S/N above 70 is sufficient to use our methods and to produce reliable stellar parameters.

We employed the IGRINS pipeline (Lee et al. 2017)[8] to reduce all the spectroscopic data. The pipeline produces a telluric corrected spectrum with a wavelength solution derived from OH night sky emission lines and telluric absorption lines. The wavelength solution was corrected for the barycenter velocity determined with ZBARYCORR (Wright & Eastman 2014).

About a third of the YSOs in our sample have more than one epoch available. For the determination of average parameters (this work) a weighted-average spectrum is produced from multi-epoch observations using the S/N at each data point as the weight. The standard deviation of the mean gives the final uncertainties per data point. Future studies of the IGRINS YSO survey will look at multi-epoch variability.

We identified binaries (or multiples) in the YSO sample with a separation of less than 2″. When the separation is greater than 2″, the objects can be observed individually by IGRINS. If the separation is less than 2″, the resultant IGRINS spectrum will contain some flux from both components. A complete determination of the binary nature of these stars is beyond the scope of this work. Binary searches for the YSOs in our sample have identified some binaries and provided limits on detection methods (Simon et al. 1995; Haisch et al. 2002; Prato et al. 2003; Ratzka et al. 2005; Prato 2007; Kraus et al. 2008; Duchêne 2010; Cieza et al. 2010; Barenfeld et al. 2019). We marked known binaries and left as singles those objects that appear as limits in binary classification studies or meet our separation criterion. Those objects that lack information in the literature have a question mark. We have excluded double-lined binaries from our sample through careful inspection of the YSO survey spectra. The binary status and basic information of our sample are available in Table 1.

3. Stellar Parameter Determination

We followed the same methods as in Paper I to obtain T, $\log g$, B, $v \sin i$, and r_K. Our method used a Markov chain Monte Carlo (MCMC) analysis as implemented in the code *emcee* (Foreman-Mackey et al. 2013). We computed a four-dimensional (T, $\log g$, B, and $v \sin i$) grid of synthetic spectra using the MOOGSTOKES code (Deen 2013).

MOOGSTOKES synthesizes the emergent spectrum of a star taking into account the Zeeman broadening produced by the presence of a photospheric magnetic field. In this work, we used the MARCS atmospheric models (Gustafsson et al. 2008) with solar metallicity (suitable for YSOs; D'Orazi et al. 2011) and the astrophysical-inferred modifications to the Vienna Atomic Line Database (Ryabchikova et al. 2015) line transition data ($\log gf$ and van der Waals constant values) presented by Flores et al. (2019). We used a microturbulence of 1 km s^{-1} as low-mass stars have microturbulence values between 0 and 2 km s^{-1} (e.g., Gray 2005; Bean et al. 2006)

Our grid of synthetic spectra matched the IGRINS spectral resolution ($R \sim 45{,}000$) and covers the parameter space as follows: from 3000–5000 K in T (steps of 100 K up to 4000 K, and 250 K above 4000 K), from 3.0–5.0 dex in $\log g$ (steps of 0.5 dex), from 0–4 kG in B (steps of 0.5 kG), and values from 2–50 km s^{-1} in $v \sin i$ (steps of 2 km s^{-1}). The grid steps[9] are spaced enough to differentiate the effects of the parameters on the spectra.

The synthetic spectral grid covers four spectral intervals in the K band, namely, Na, Ti, Ca, and CO. The intervals include neutral atomic (Fe, Ca, Na, Al, and Ti) and molecular lines (CO) that are sensitive to changes in the different stellar parameters (see Figure 2 of Paper I). The four spectral intervals are shown in Figure 1. Each spectral region was normalized using an interactive Python script. The script fits a polynomial of order n to a custom number of flux bins, usually between 10 and 20 bins, and a polynomial of order 1–4. After normalizing the continuum, we carried out the MCMC trial comparing observed and synthetic spectra in the K-band spectral regions by allowing T, $\log g$, B, $v \sin i$, and veiling to vary along with small continuum (<6%) and wavelength (<1.0 Å) offsets. In each MCMC trial, we linearly interpolated within the four-dimensional (T, $\log g$, B, and $v \sin i$) synthetic spectral grid to obtain the corresponding spectrum with the sampled set of parameters. The interpolated synthetic spectrum was then artificially veiled by the veiling parameter and re-normalized for each region. A single veiling value was used for all the K-band wavelength regions.

Finally, from the posterior probability distributions of the MCMC, we took the 50th percentile as the most likely value for

[6] An A0V telluric standard star was observed at a similar airmass within 2 hr before or after the science target.

[7] https://wikis.utexas.edu/display/IGRINS/SNR+Estimates+and+Guidelines

[8] https://github.com/igrins/plp/tree/v2.1-alpha.3

[9] The grid steps of T and $\log g$ are defined by the model atmosphere, while we selected the steps of B and $v \sin i$.

Table 1
Basic Information and Results for Our Ophiuchus and Upper Scorpius Sample

2MASS	Name	N	K mag	SpT	ref	cluster	Ref	Bin	Ref	A_V mag	α_{K_s-W4}	Flag	T K	$\log g$ dex	B kG	$v \sin i$ km s^{-1}	r_K
J16081474-1908327	EPIC 205152548	2	8.4	K2	18	USco	14	Y	16	0.6 ± 0.1	-2.79 ± 0.06	1	4652 ± 172	4.55 ± 0.34	1.05 ± 0.70	8.4 ± 3.8	0.31 ± 0.15
J16082324-1930009	EPIC 205080616	1	9.5	K9	18	USco	14	N	8	0.8 ± 0.5	-1.09 ± 0.22	1	3782 ± 277	4.16 ± 0.44	2.03 ± 0.91	14.3 ± 4.1	0.15 ± 0.11
J16090075-1908526	EPIC 205151387	2	9.2	M1	18	USco	14	N	8	0.7 ± 0.5	-0.70 ± 0.27	0	3636 ± 188	4.22 ± 0.32	1.88 ± 0.45	8.8 ± 2.9	0.26 ± 0.09
J16093030-2104589	RX J1609.5-2105	1	8.9	M0	18	USco	15	N	16	0.6 ± 0.6	-2.75 ± 0.04	0	4021 ± 278	3.98 ± 0.47	1.44 ± 0.90	10.7 ± 3.9	0.20 ± 0.11
J16110890-1904468	ScoPMS 44	4	7.7	K4	18	USco	15	N	16	1.4 ± 0.2	-2.78 ± 0.07	1	4220 ± 160	4.50 ± 0.33	<2.66	27.1 ± 3.4	0.44 ± 0.09
J16113134-1838259	V* V866 Sco	10	5.8	K5	18	USco	14	Y	3	3.4 ± 0.5	-0.49 ± 0.05	1	3919 ± 230	3.49 ± 0.39	<1.52	16.5 ± 3.6	7.45 ± 1.00
J16142029-1906481	EPIC 205158239	1	7.8	M0	18	USco	14	N	13	2.8 ± 0.8	-0.71 ± 0.07	1	3911 ± 391	4.13 ± 0.60	<1.97	24.5 ± 8.3	1.64 ± 0.53
J16153456-2242421	V* VV Sco	1	7.9	M0	18	USco	15	Y	8	1.2 ± 0.7	-0.92 ± 0.22	1	3685 ± 356	4.17 ± 0.56	2.47 ± 1.05	10.2 ± 5.9	1.16 ± 0.31
J16211848-2254578	EPIC 204290918	1	10.2	M2	18	USco	14	N	11	2.1 ± 0.7	-0.84 ± 0.16	0	3414 ± 229	4.09 ± 0.45	<1.51	19.4 ± 3.4	0.67 ± 0.16
J16220961-1953005	EPIC 205000676	1	8.9	M3.7	17	USco	14	Y	16	1.6 ± 0.7	-2.08 ± 0.09	1	3371 ± 228	3.80 ± 0.40	<1.24	16.1 ± 2.9	0.19 ± 0.11
J16232454-1717270	EPIC 205483258	3	9.7	M2.5	18	USco	15	?	…	…	…	3	…	…	…	…	…

Note. The "Flag" columns listing 0, 1, 2, and 3 indicate the good, acceptable, at the edge of the grid, and bad determinations of atmospheric parameters. The K magnitude is from Cutri et al. (2003). The full version of this table is available in the online version of this paper.

References. (1) Simon et al. (1995) (2) Haisch et al. (2002) (3) Prato et al. (2003) (4) Ratzka et al. (2005) (5) Wilking et al. (2005) (6) Torres et al. (2006) (7) Prato (2007) (8) Kraus et al. (2008) (9) Ricci et al. (2010) (10) Duchêne (2010) (11) Cieza et al. (2010) (12) Hsieh & Lai (2013) (13) Lafreniére et al. (2014) (14) Rebull et al. (2018) (15) Luhman et al. (2018) (16) Barenfeld et al. (2019) (17) Esplin & Luhman (2020) (18) Luhman & Esplin (2020).

(This table is available in its entirety in machine-readable form.)

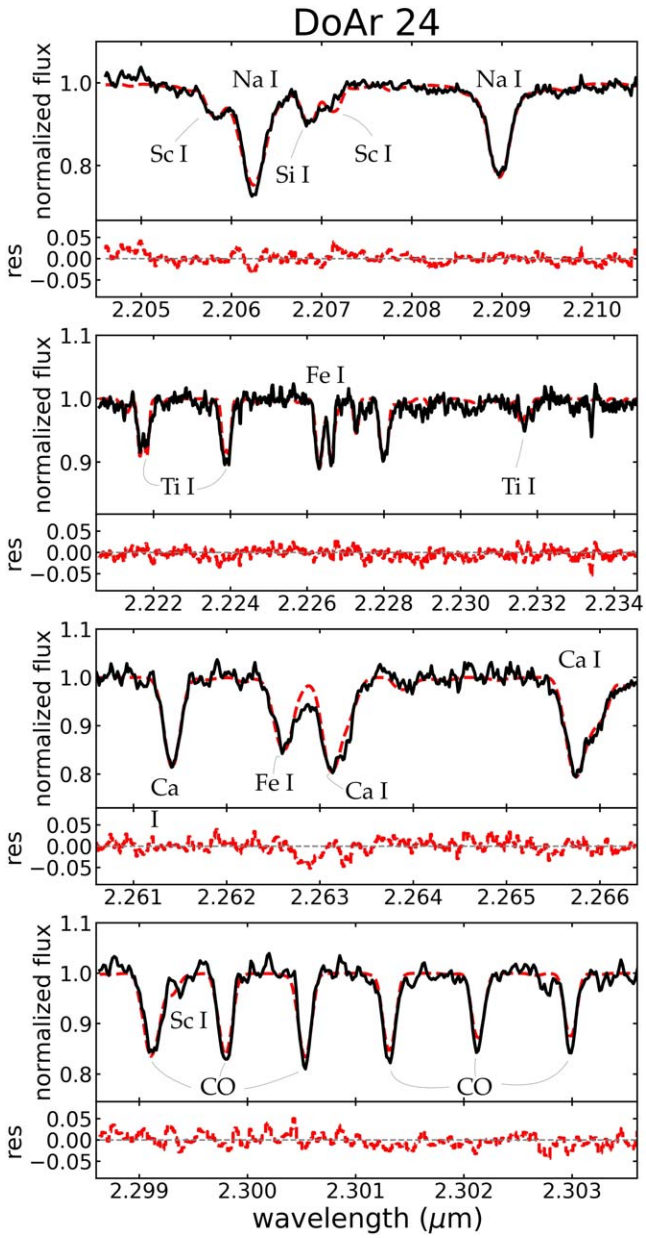

Figure 1. The spectral regions used in this work for the star DoAr 24 (solid black line, 2MASS J16261706-2420216). We included the best-fit synthetic spectrum (red-dashed line), which has $T = 4092$ K, $\log g = 4.11$ dex, $B = 2.12$ kG, $v \sin i = 10.6$ km s^{-1}, and a K-band veiling of 0.79. The bottom panels show the residuals between the observed and the synthetic spectra. The level of agreement between the best-fit synthetic spectrum and the DoAr 24 observed spectrum was considered a good determination. We also indicate some atomic and molecular lines present in the spectral regions.

each stellar parameter. We computed the total uncertainty for each parameter as the quadrature sum of the formal fit errors (the larger of the 16th and 84th percentiles of the posterior probability distribution) and the systematic errors. The systematic errors were determined in Paper I and we assume the same values for this work. They are 75 K, 0.13 dex, 0.26 kG, and 1.7 km s^{-1} for T, $\log g$, B, and $v \sin i$, respectively.

4. Results

Once we determined the stellar parameters of our sample (Table 1), we categorized our determinations, based on a visual inspection and χ^2 statistics, with a numerical quality flag equal to 0, 1, or 3 if they are good, acceptable, or poor determinations. We identified objects with lower/upper limits outside or at the edge of our grid with a flag of 2. We used each stellar parameter's total uncertainty to compute its lower and upper limits. In Figure 1, we show an illustrative example of how the synthetic spectra reproduce the observations.

We identified 31, 25, 5, and 9 stars whose parameters are good, acceptable, at the edge of the grid or poor determinations, respectively. We excluded poor determinations in our further analysis and referred to the 61 remaining stars as our sample.

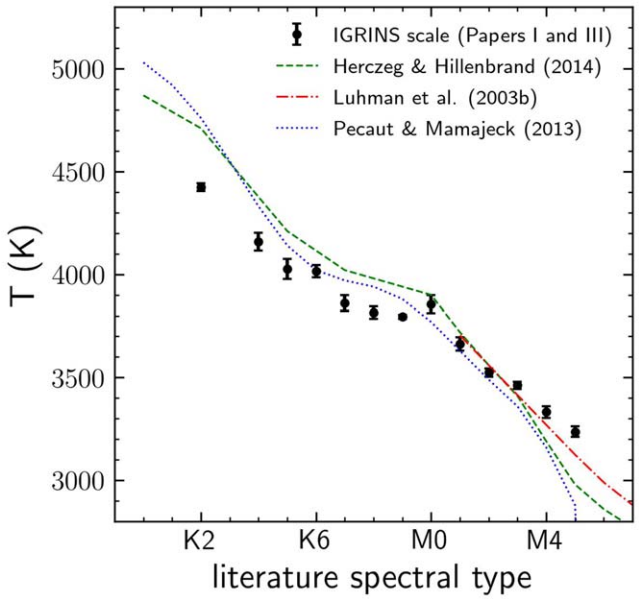

Figure 2. Temperature as a function of the literature spectral type. The dots represent the IGRINS temperature scale, determined using the temperatures obtained for the nonbinary YSOs of Ophiuchus, Upper Scorpius, TWA, and Taurus. The different lines represent the temperature scales of Herczeg & Hillenbrand (2014), Luhman et al. (2003), and Pecaut & Mamajek (2013). Our temperature scale agrees with the published temperature scales for the M0–M3 stars but follows the Luhman et al. (2003) scale for late types. However, our temperatures are cooler than the published scales in K stars. The error bar in our temperature is the standard deviation of the mean within the ±0.5 spectral type subclasses.

4.1. Photospheric Temperature

The derived temperatures for nonbinary Ophiuchus and Upper Scorpius YSOs follow the same trend with spectral type as was found for single Taurus YSOs in Paper I. To improve our previous IGRINS temperature scale, we combined our previous T values of Taurus and TWA (Paper I) with the T determinations made in this work. The combined sample (Paper I and this work) comprises 190 YSOs.

We computed the mean T and the standard deviation of the mean in bins of ±0.5 spectral type subclasses to construct the IGRINS temperature scale. We included in our IGRINS temperature scale spectral type bins with more than one object.

In Figure 2, we compare the updated IGRINS temperature scale, which is in Table 2, to the published scales of Pecaut & Mamajek (2013), Herczeg & Hillenbrand (2014) and Luhman et al. (2003). In general, the shape of our temperature scale is similar to the published ones. The T values for M0–M3 stars agree with the three temperature scales. However, our scale agrees better with the Luhman et al. (2003) for late spectral types. For the K stars, we found that our temperature values are

Table 2
Temperature Scale Determined Using IGRINS Data Along with Those of Luhman et al. (2003, L03), (Pecaut & Mamajek (2013, PM13), and (Herczeg & Hillenbrand (2014, HH14)

SpT	L03 (K)	PM13 (K)	HH14 (K)	IGRINS (K)	N
K0	⋯	5030	4870	⋯	⋯
K1	⋯	4920	⋯	⋯	⋯
K2	⋯	4760	4710	4424 ± 18	2
K3	⋯	4550	⋯	⋯	⋯
K4	⋯	4330	⋯	4158 ± 43	2
K5	⋯	4140	4210	4025 ± 49	5
K6	⋯	4020	⋯	4016 ± 30	14
K7	⋯	3970	4020	3861 ± 37	4
K8	⋯	3940	⋯	3815 ± 29	5
K9	⋯	3880	⋯	3795 ± 9	2
M0	⋯	3770	3900	3856 ± 43	15
M1	3705	3630	3720	3663 ± 33	16
M2	3560	3490	3560	3525 ± 20	16
M3	3415	3360	3410	3462 ± 18	19
M4	3270	3160	3190	3332 ± 29	16
M5	3125	2880	2980	3237 ± 26	11

Note. This IGRINS temperature scale is an update of that presented in Paper I. The last column lists the number of objects for which we computed the mean T value and the standard error of the mean within ±0.5 spectral type subclasses. We only included spectral type bins with more than one determination.

cooler than the temperature scales found in Pecaut & Mamajek (2013) and Herczeg & Hillenbrand (2014).

The differences between our T values and those in the literature could be an effect of having a small sample of K stars. Also, it can be explained as a cumulative result of using different atmospheric models and line lists, different methodologies (spectroscopy versus photometry), different wavelength intervals (optical versus infrared), the effect of the B field on T, and even differing SpT classifications.

For example, typical SpT uncertainties are about one subclass (∼100 K); however, in many cases, the SpT determined by different groups for a certain YSO disagrees by more than two subclasses, even more than five in extreme cases. Additionally, omitting the B field in the T determination produces temperatures, on average, ∼40–70 K cooler than if the B is considered (Paper I).

One way that we reduce SpT uncertainties in this work is to use homogeneous SpT classifications. The SpT of the Taurus sample comes from Luhman et al. (2017), while for Ophiuchus and Upper Scorpius members, the SpT comes mostly from Esplin & Luhman (2020) and Luhman & Esplin (2020). These three studies measured SpT by comparing absorption bands (TiO, VO, Na I, K I, and H_2O) between observed and standard optical and infrared spectra. Their reported uncertainties in SpT are ± 0.25 and ± 0.5 subclasses for optical and infrared types.

4.2. Surface Gravity

The log g distributions of Ophiuchus and Upper Scorpius are differentiated in Figure 3. Their Kolmogorov–Smirnov (K-S) probability[10] of 0.1% also shows that they are statistically different. The Ophiuchus distribution has a mean log g (and

[10] The K-S test computes the probability that two populations come from the same parent distribution.

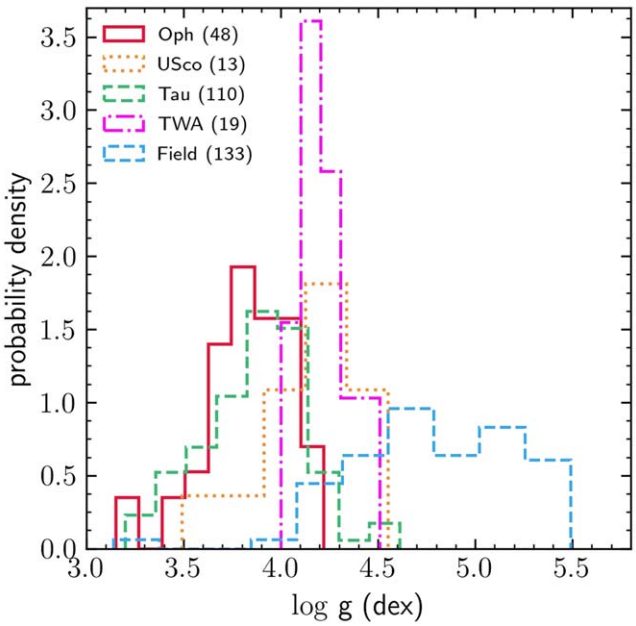

Figure 3. Probability density of log g for 48, 13, 110, and 19, YSOs members of Ophiuchus, Taurus, Upper Scorpius, and TWA. We also show the log g determinations obtained for 133 K and M field stars.

error on the mean) of 3.83 ± 0.03 dex, while Upper Scorpius has 4.13 ± 0.08 dex.

Considering the log g as a proxy for age, we can speculate that such differences in log g between samples might be due to age. To test this, we used the combined sample, and we also included the log g values determined for 133 field stars (see Appendix A.2) as a more evolved counterpart.

From Figure 3, we can see that the log g distributions of Taurus and Ophiuchus are very similar as its K-S probability of 78% also confirms. We also found that the log g distribution of Upper Scorpius is comparable to the TWA distribution (K-S probability of 35%).

We can also see in Figure 3 that the log g distribution of field stars is distinguishable from the YSOs, as is expected for a more evolved sample. There is some overlapping between the low log g values of the field stars, which is about 4.0 dex, and the higher log g determinations of Taurus, Ophiuchus, Upper Scorpius, and TWA.

Based on our log g determinations and using them as an age proxy, we can conclude that Ophiuchus and Taurus have a similar age, which is younger than the indistinguishable Upper Scorpius and TWA samples.

In Figure 4, we produce the Kiel (T versus log g) diagram for the YSOs in Taurus, Ophiuchus, Upper Scorpius, and TWA. We also included in Figure 4 the magnetic evolutionary models of Feiden (2016) as a theoretical comparison. The Taurus and Ophiuchus objects seem to populate similar parts of the Kiel diagram, and there is no clear difference in log g between them. These objects also have a larger log g dispersion than their counterparts in Upper Scorpius or TWA.

4.3. Spectral Indices and Classification

Based on the shape of their de-reddened spectral energy distributions (SEDs), Lada & Wilking (1984) divided the YSOs into three different morphological classes (I, II, and III), by means of the spectral index $\alpha = d\log(\lambda F_\lambda)/d\log\lambda$.

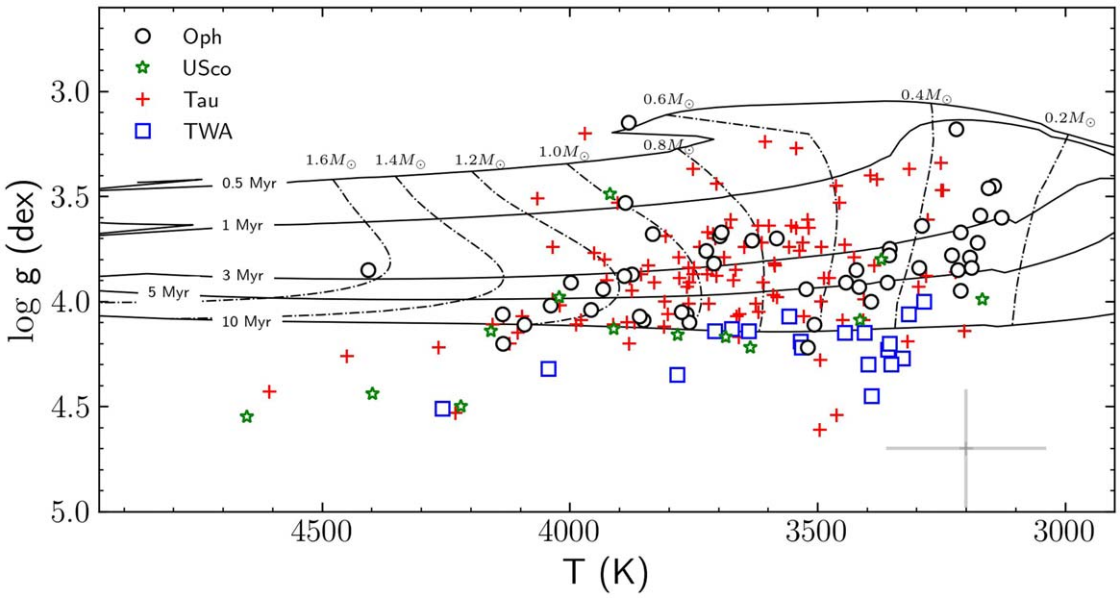

Figure 4. Spectroscopic Hertzprung–Russell or Kiel diagram for 48 Ophiuchus (circles), 110 Taurus-Auriga (plus), 13 Upper Scorpius (stars), and 19 TWA (squares) YSOs. The Taurus and Ophiuchus samples seem to populate similar parts of this diagram, and it is no clear difference in log g. Some objects of Upper Scorpius and Taurus have a log g value relatively high compared with most of our determinations. We included magnetic evolutionary tracks of Feiden (2016). Finally, the error bar in the right-bottom corner represents the median uncertainties of our combined sample.

The class scheme represents an evolutionary sequence of low-mass stars, and it is helpful to understand the star formation process. Although most of our YSOs have a previous classification, we computed de-reddened α indices for our YSOs to investigate trends with stellar parameters.

We first constructed the infrared SED from the Two Micron All Sky Survey (2MASS; J, H, and K_s) and Wide-field Infrared Survey Explorer (WISE; W1, W2, W3, and W4) magnitudes reported in the ALLWISE catalog (Cutri et al. 2021). We included those magnitudes with a flux signal-to-noise ratio greater than 2 and ignored the upper limits.

We then corrected the observed SEDs by reddening. We used a visual extinction (A_V) estimation that we converted into a extinction in the K_s band (A_{K_s}) by means of $A_{K_s}/A_V = 0.112$ (Rieke & Lebofsky 1985; Großschedl et al. 2019). We then employed the zero magnitude flux densities, and extinction laws reported in Indebetouw et al. (2005) and Großschedl et al. (2019) to compute the de-reddened J, H, K, W1, W2, W3, and W4 fluxes. Using the de-reddened fluxes and the central wavelengths of each filter, we created the extinction-corrected infrared SED for those YSOs in our combined sample with A_V estimations. We obtained A_V values with the code MassAge (J. Hernández et al. 2023, in preparation). MassAge input includes T, Gaia EDR3 (Gp, Rp, and Bp), and 2MASS (J and H) photometry to compute A_V by minimizing the differences between the observed and expected intrinsic colors of Luhman & Esplin (2020) affected by reddening. The reddening A_V is changed until the best comparison is found using the minimal χ^2 method.

The uncertainties in A_V values are obtained using the Monte Carlo method of error propagation (Anderson 1976), assuming Gaussian distributions for the uncertainties in the input parameters. We found photometric data for only 171 objects, for which we computed the A_V (see Table 1).

Continuum veiling (r_K) and A_V affect the stellar light similarly, i.e., they redden it. Since we determine T by taking into account r_k, we ensure that MASSAGE is correctly determining the A_V values. Moreover, if we compare the r_k values as a function of their MassAge A_V we do not find any trend. Furthermore, these data have a correlation coefficient of 0.18, suggesting a weak correlation between our r_k and A_V values.

The presence, structure, accretion status, and evolutionary state of a circumstellar disk impact the photometric colors, producing an incorrect A_V value. As some of our YSOs might still possess a disk, we ran MassAge a second time. This time we did not include the Gaia Bp magnitude, which should be the photometric band most affected by the accretion, to assess the impact of accretion in our sample. We found that the A_V obtained using all the photometric bands are higher, on average 0.14 mag, than those values determined ignoring Bp magnitude. This difference is lower than the mean uncertainty determined for A_V, which is about 0.4 mag.

Finally, to obtain the infrared spectral index (α_{K_s-W4}) we perform a linear fit between the K_s and W4 de-reddened fluxes. Our infrared indices are reported in Tables 1 and 3.

As a quality check, in Figure 5, we compared our spectral indices with those determined by Dunham et al. (2015) and Luhman et al. (2010) for YSOs in the Ophiuchus and Taurus star-forming regions, respectively. Dunham et al. (2015) determined the spectral index α through a linear least-squares fit of all available 2MASS and Spitzer photometry between 2 and 24 μm. On the other hand, Luhman et al. (2010) computed the spectral index between four pairs of photometric bands, including the pair K_s and Spitzer 24 μm. These spectral indices are compatible with those determined here, as we obtained them from the same wavelength range (2–24 μm). The only difference between the works of Dunham et al. (2015), Luhman et al. (2010), and ours is that we used WISE photometry instead of Spitzer.

Our classifications are consistent with the literature. For Taurus, we found that α_{K_s-W4} values are around the one-to-one line for the entire interval. On the other hand, our Ophiuchus α indices are higher than those determined by Dunham et al. (2015), on

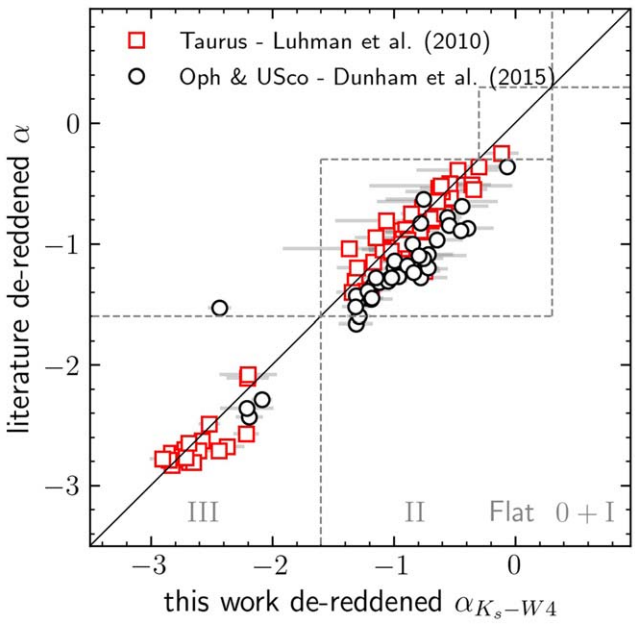

Figure 5. Comparison of the de-reddened α indices determined in this work with those determined in Dunham et al. (2015) and Luhman et al. (2010). The gray squares represent the area where they agree on the class status. We used the classification thresholds of Großschedl et al. (2019) for Class III, Class II, Flat spectrum, and Class 0+I, respectively. The error bar on our determinations is the uncertainty in the best-fit slope. Our indices are in good agreement for Taurus, but they present a systematic offset toward higher values (on average, +0.25) for Ophichus YSOs. The reason for this offset is unclear but might be related to using different photometric data, zero-points, and extinction laws.

average, ∼0.25. The source of this discrepancy is unclear but is likely related to the difference between the WISE and Spitzer photometry and the use of different photometric zero-points and extinction laws.

4.4. Spectral Indices versus Stellar Parameters

Once we homogeneously computed $\alpha_{K_s-\mathrm{W4}}$ values, we looked for trends between them and the determined stellar parameters. As we mentioned before, the α index informs us of the evolutionary status of the YSO.

We did not find any correlation between $\alpha_{K_s-\mathrm{W4}}$ and T. The dispersion of the T values in the four populations is very similar, and also between Class II and Class III YSOs.[11] Regarding $\log g$, we found that, on average, $\log g$ values of Class III are higher than their Class II counterparts. We found a mean and standard deviation of the mean for Class II YSOs of 3.86 ± 0.02 dex, while for Class III we found 4.02 ± 0.04 dex.

Similarly, we found that $v \sin i$ values of Class III are slightly higher than those of Class II. We found a mean value of $15.0 \pm 0.7\,\mathrm{km\,s^{-1}}$ and $18.2 \pm 1.4\,\mathrm{km\,s^{-1}}$ for the Class II and Class III YSOs, respectively. This result can be related to the disk locking scenario in which the presence of an accretion disk regulates the stellar rotation (Serna et al. 2021).

We consider 65 B determinations from Taurus, Ophiuchus, Upper Scorpius, and TWA. We did not find any trend with the $\alpha_{K_s-\mathrm{W4}}$ values and the B field. Both Class II and Class III YSOs have B fields very similar between them. We found a mean value of 1.96 ± 0.06 kG for Class II and 2.04 ± 0.15 kG for Class III YSOs, respectively.

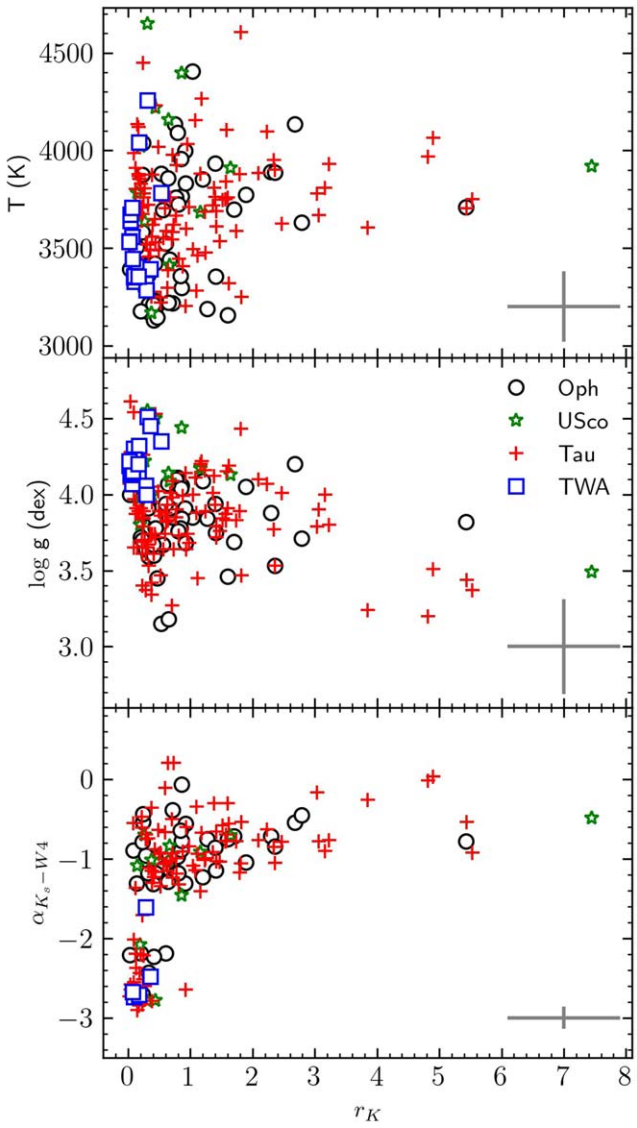

Figure 6. Comparison between the K-band veiling and T (top), $\log g$ (middle), and $\alpha_{K_s-\mathrm{W4}}$ (bottom) for the Ophiuchus (black circles), Upper Scorpius (green stars), Taurus (red crosses), and TWA (blue squares). The veiling values of Taurus, Ophiuchus, and Upper Scorpius are more spread out than those of TWA. We also included in each panel the mean error bar.

The strongest and expected trend of $\alpha_{K_s-\mathrm{W4}}$ is seen for the K-band veiling values (see Figure 6). More evolved objects have lower K-band veiling values ($r_K \lesssim 0.6$). Interestingly, the K-band veiling values show a large dispersion for Class II YSOs. Such a distribution could be related to the variable nature of the Class II YSOs or intrinsic differences between the YSOs.

We also compared T and $\log g$ with the K-band veiling in Figure 6. We can see that the TWA objects have a K-band veiling less than ∼0.8. The veiling values of Taurus, Ophiuchus, and Upper Scorpius are more spread out than those of TWA. Most are between 0 and 3.2, while a few YSOs have K-band veiling greater than 3.2 and up to ∼7.3.

Although of low significance, there seems to be a trend toward higher r_K as the $\log g$ decreases. The latter suggestion implies that less evolved objects have high veiling values., which aligns with the idea that the veiling is related to the

[11] We used the classification thresholds of Großschedl et al. (2019) and our $\alpha_{K_s-\mathrm{W4}}$ values. Class II: $-1.6 < \alpha < -0.3$; Class III: $\alpha \leqslant -1.6$.

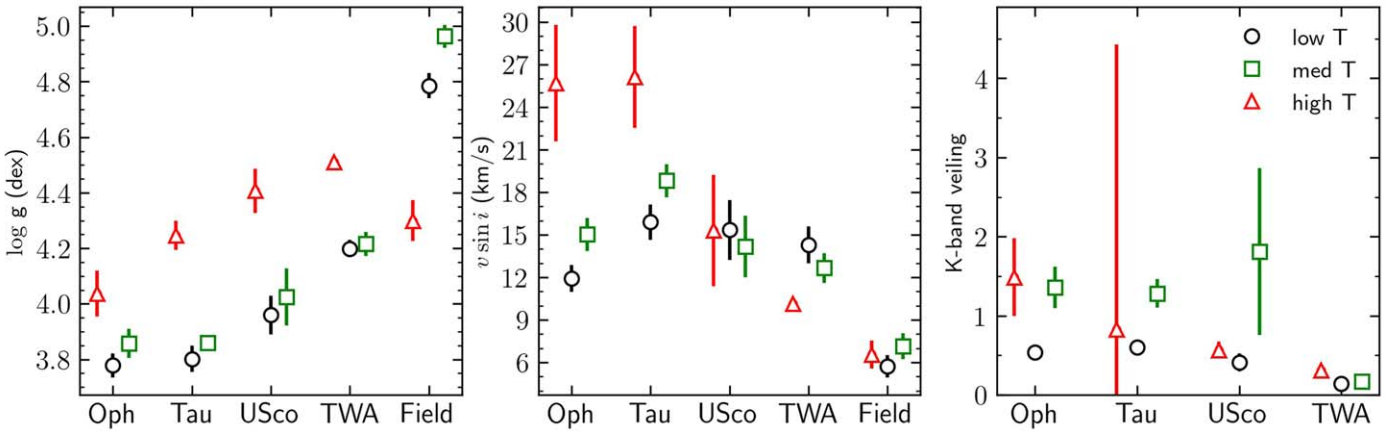

Figure 7. Mean $\log g$, $v \sin i$, and K-band veiling as a function of T bins and by star-forming region. The YSOs of Taurus, Ophiuchus, Upper Scorpius, and TWA are divided into low (circles, $3100 \leqslant T < 3600$ K), med (squares, $3600 \leqslant T < 4100$ K), and high (triangles, $T \geqslant 4100$ K) temperature bins. The error bar is the standard error on the mean ($\sigma/\sqrt{n}$) of each T bin. We also included in the left and middle panels the field stars.

presence of a circumstellar disk. Also, this behavior might be due in part to a degeneracy between r_K and $\log g$, as their effects on the spectral lines are similar.

In terms of T, between ∼3600 and ∼4100 K, the r_K could be as high as ∼7.3. This differs from other temperature ranges, where the highest K-band veiling is around 2.

4.5. Magnetic Field

The ability to determine the B field from the Zeeman broadening is related directly to the spectral resolution and the $v \sin i$ of the star. Based on the results of Hussaini et al. (2020), the minimum B field we can detect from IGRINS spectra should be greater than 1.0 kG, and this scales with the $v \sin i$ as $B \geqslant v \sin i/8$ (kG/km s^{-1}). We consider B values that do not meet this criterion to be a non-detection. We found that seven and 20 B-field values meet the detection threshold in the Upper Scorpius and Ophiuchus star-forming regions, respectively. The Kolmogorov–Smirnov probability computed between the two samples of B-field determinations is 50%, which means that both samples are not statistically different at that level. In Table 1 we report both determinations and limits for the B field of our targets.

The combined sample (Paper I and this work) has 78 B-field determinations (20 in Ophiuchus, seven in Upper Scorpius, 41 in Taurus, and 10 in TWA) and 112 B-field limits. We have compared stellar parameters for the YSOs with B-field detections and non-detections looking for possible trends. In terms of T, we found that the mean T for the B-field determinations and B-field limits is very similar, 3675 and 3655 K, respectively. This result suggests that the two groups are indistinguishable in terms of T, as it is also confirmed by their K-S test probability of 35%. In terms of K-band veiling, we found a K-S probability of 5% with a mean K-band veiling for the B-field determinations of 0.88 and the B-field non-detections of 0.92. We then focused on the B-field determinations and split our 78 determinations into two B-field strength bins: low B field ($1 \leqslant B <$2.0 kG) and high B field ($B \geqslant$2.0 kG). According to the K-S probability, the low and high B-field distributions are statistically the same for T and K-band veiling at 40% and 14%, respectively.

Interestingly, we found a mean $\log g$ of 3.88 and 4.08 dex for the low B- and high B-field bins, respectively. We also found a K-S probability of about 1%, meaning that both strength bins are different in terms of $\log g$. This is the expected behavior if most of the B field comes from primordial field conservation during radius contraction of pre-main-sequence stars (Moss 2003).

4.6. Temperature Bins

The homogeneous stellar parameter determination that we perform for the YSOs in Ophiuchus, Upper Scorpius, Taurus, and TWA, along with the field stars, allowed us to analyze the similarities and differences of these samples from an evolutionary point of view.

As we see in the previous sections, there are differences between the YSO populations in their $\log g$ distributions, which we attribute to differences in age. However, the stellar mass plays a crucial parameter in the evolution of the stars. T is a rough proxy for stellar mass in most evolutionary models, as constant mass tracks are primarily vertical in the Kiel diagram (e.g., Figure 4).

For that reason, and to fully understand if the differences found in $\log g$ are due to age, we separated our star-forming regions into three different T bins. Our YSO T values span a range of ∼1500 K, between ∼3100 and ∼4600 K, so our bins comprise stars within 500 K. We name our bins as low ($3100 \leqslant T < 3600$ K), med ($3600 \leqslant T < 4100$ K), and high ($T \geqslant 4100$ K) temperature, and they contain 82, 92, and 16 objects, respectively. In Figure 7, we show how the $\log g$, $v \sin i$, and K-band veiling behave in each mass bin and each star-forming region. We also include field stars in the $\log g$ and $v \sin i$ analysis.

In the four star-forming regions, the behavior with $\log g$ (left panel Figure 7) is the same. Objects in the low and med T bins have lower mean $\log g$ values than those in the high T bin. However, in the field stars, the high T bin has low mean $\log g$ values. According to the evolutionary tracks of Marigo et al. (2017), for an age of ∼500 Myr, stars with T between 3000 and 4000 K (roughly our low and med T bins) have $\log g$ values ranging from ∼5.0 to 4.7 dex, while stars with K spectral types (high T bin) have $\log g$ in the range of ∼4.66–4.63 dex. Our $\log g$ values agree with the theoretical predictions of Marigo et al. (2017) for the M stars. However, our results for the K stars are lower by ∼0.3 dex than such predictions. Considering that $\log g$ is a challenging parameter to determine, we need a more detailed analysis of the field star sample to address the

source of this $\log g$ discrepancy in the K stars, which is beyond the scope of this paper. Our $\log g$ values follow the trend of the theoretical predictions where K stars have higher $\log g$ than M stars, and they are helpful in the relative sense we have used them throughout the paper. We see from the middle panel of Figure 7 that the mean $v \sin i$ values create a descending ladder of the mean $v \sin i$ values in the following order: Taurus, Ophiuchus, Upper Scorpius, TWA, and field stars. Finally, the mean values of the K-band veiling (right panel Figure 7) are very similar between T bins and between star-forming regions.

5. Summary and Conclusions

Using high signal-to-noise K-band spectra obtained with IGRINS and an MCMC approach to spectral fitting, we determined stellar parameters for a sample of 61 YSOs in the Ophiuchus and Upper Scorpius complexes. We also determined the stellar parameters for some K and M field stars reported in López-Valdivia et al. (2019). We simultaneously fit four observed spectral regions with a synthetic spectral grid computed with solar metallicity MARCS models and the spectral synthesis code MOOGSTOKES to obtain T, $\log g$, $v \sin i$, r_K, and B-field strength. Our B-field determination relies on the Zeeman broadening, whose detection is limited by the $v \sin i$ of the star and the spectral resolution. For this reason, we determined B just for 27 YSOs and provided limits on the B field for the remaining stars in the sample.

We found that our temperatures for M0–M3 stars agree with three published temperature scales (Luhman et al. 2003; Pecaut & Mamajek 2013; Herczeg & Hillenbrand 2014). For late M stars, our T values agree more with those of Luhman et al. (2003) while for K stars, we found that our temperatures are colder than the temperature scales of Pecaut & Mamajek (2013) and Herczeg & Hillenbrand (2014). The differences in the T can be explained as a cumulative result of small number statistics, differences in the employed methodology, use of different atmospheric models, line lists, and wavelength intervals, the effect of the B field on T, and inconsistent spectral type classifications.

We found that the mean $\log g$ value of Ophiuchus (3.83 ± 0.03 dex) is similar to that of Taurus (3.87 ± 0.03 dex), while the mean $\log g$ of Upper Scorpius (4.13 ± 0.08 dex) is similar to the value found for TWA (4.22 ± 0.03 dex). If we consider $\log g$ as a proxy for age, our results suggest that the Ophiuchus and Taurus samples have a similar age. We also find that Upper Scorpius and TWA YSOs have similar ages, and are more evolved than Ophiuchus/Taurus YSOs. We derived visual extinction and gathered from literature 2MASS and WISE photometry to construct de-reddened infrared SEDs for our sample. We compute spectral indices and classify our YSO samples into morphological classes with these SEDs. In the combined sample of YSOs, which includes objects from Ophiuchus, Taurus, Upper Scorpius, and TWA, we found that Class II YSOs have, on average, lower $\log g$ and $v \sin i$, similar B field, and higher K-veiling values than their Class III counterparts.

We appreciate the detailed comments from the anonymous referee, which improved the science and text of this manuscript. This work used IGRINS, which was developed under a collaboration between the University of Texas at Austin and the Korea Astronomy and Space Science Institute (KASI) with the financial support of the US National Science Foundation under grant Nos. AST-1229522 and AST-1702267, of the University of Texas at Austin, and of the Korean GMT Project of KASI. R.L.V. acknowledges support from CONACYT through a postdoctoral fellowship within the program Estancias Posdoctorales por México. This paper includes data taken at The McDonald Observatory of The University of Texas at Austin. These results made use of the Lowell Discovery Telescope. Lowell is a private, nonprofit institution dedicated to astrophysical research and public appreciation of astronomy and operates the LDT in partnership with Boston University, the University of Maryland, the University of Toledo, Northern Arizona University, and Yale University. Based on observations obtained at the Gemini Observatory, which is operated by the Association of Universities for Research in Astronomy, Inc., under a cooperative agreement with the NSF on behalf of the Gemini partnership: the National Science Foundation (United States), the National Research Council (Canada), CONICYT (Chile), Ministerio de Ciencia, Tecnología e Innovación Productiva (Argentina), and Ministério da Ciência, Tecnologia e Inovação (Brazil). This material is based upon work supported by the National Science Foundation under grant No. AST-1908892 to G.M.

Software: IGRINS pipeline package (Lee et al. 2017), `MoogStokes` (Deen 2013), `MARCS` models (Gustafsson et al. 2008), `zbarycorr` (Wright & Eastman 2014), `MassAge` (J. Hernández et al. 2023, in preparation).

Appendix
Stellar Parameters of Taurus, TWA, and Field Stars

A.1. Taurus and TWA

We included in this work the Taurus and TWA YSOs analyzed in Paper I. We compare their stellar parameters to establish similarities and differences between these four YSO populations.

In Table 3, we gathered the stellar parameters reported in Paper I for the Taurus and TWA YSOs. We also added the values of A_V and α_{K_s-W4} computed in this work for many of them.

A.2. Field Stars

Between 2014 and 2018, as part of various scientific projects, IGRINS observed 254 K and M field stars at the McDonald Observatory 2.7 m telescope, Lowell Discovery Telescope, and Gemini South Telescope. López-Valdivia et al. (2019) presented an accurate determination of their temperatures using absorption line-depths of Fe I, OH, and Al I, located at the H-band and BT-Settl models (Allard et al. 2013).

These K and M stars are an excellent sample of more evolved counterparts for our YSO sample. The field stars allow us to complete the age ladder we are creating with the IGRINS YSO survey, establish the differences or similarities between the populations at different evolutionary stages, and identify the role of the stellar parameters at every step.

We started selecting from López-Valdivia et al. (2019) just the stars with spectral type between K0 and M5 and with a minimum mean signal-to-noise ratio of $\sim$50 in the K band, finishing with a sample of 207 field stars. Then, we determined the stellar parameters in the field stars following the MCMC approach as in our YSO sample, but with minor variations.

The main differences between the MCMC applied to the field stars and the YSOs are that (i) due to the more evolved status of the field stars, there is no need to include any K-band veiling contribution, so we removed this free parameter from

Table 3
Stellar Parameters for Taurus and TWA YSOs

2MASS	SpT	Cluster	A_V mag	α_{K_s-W4}	Flag	T K	$\log g$ dex	B kG	$v \sin i$ km s^{-1}	r_K
J04043984+2158215	M3.2	Tau	0.7 ± 0.6	-2.6 ± 0.0	1	3461 ± 216	4.54 ± 0.35	2.75 ± 0.60	17.7 ± 3.4	0.09 ± 0.06
J04053087+2151106	M2.7	Tau	0.6 ± 0.6	-2.6 ± 0.0	1	3496 ± 183	4.61 ± 0.24	3.21 ± 0.39	5.0 ± 2.4	0.04 ± 0.03
J04131414+2819108	M3.6	Tau	0.4 ± 0.4	-2.8 ± 0.1	0	3393 ± 154	3.40 ± 0.24	<1.43	31.2 ± 2.3	0.23 ± 0.06
J04132722+2816247	M0.5	Tau	2.6 ± 0.3	-2.8 ± 0.1	1	3875 ± 181	3.95 ± 0.34	<2.49	27.3 ± 4.0	0.38 ± 0.11
J04141358+2812492	M4.5	Tau	0.9 ± 0.5	-0.6 ± 0.2	0	3318 ± 220	4.19 ± 0.42	2.67 ± 0.60	9.7 ± 3.2	1.62 ± 0.21
J04141458+2827580	M3.5	Tau	0.8 ± 0.5	-0.4 ± 0.2	0	3251 ± 157	3.34 ± 0.27	1.14 ± 0.33	4.6 ± 2.3	0.37 ± 0.08
J04141760+2806096	M5.0	Tau	1.9 ± 0.6	-0.3 ± 0.1	0	3281 ± 196	3.88 ± 0.40	<1.09	9.9 ± 2.9	1.10 ± 0.21
J04143054+2805147	M2.2	Tau	5.1 ± 0.6	0.2 ± 0.1	0	3620 ± 186	3.64 ± 0.34	<2.36	22.7 ± 3.9	0.73 ± 0.12
J04144730+2646264	M2.6	Tau	0.7 ± 0.8	-1.2 ± 0.2	0	3530 ± 257	3.72 ± 0.42	<1.72	31.0 ± 4.2	0.44 ± 0.15
J04144786+2648110	M2.5	Tau	0.5 ± 0.5	-0.7 ± 0.2	0	3520 ± 180	3.61 ± 0.30	<1.39	20.5 ± 2.5	0.28 ± 0.08
J04144928+2812305	M3.5	Tau	1.6 ± 0.3	-0.9 ± 0.1	0	3246 ± 104	3.47 ± 0.21	<1.03	11.1 ± 1.9	0.52 ± 0.06
J04154278+2909597	M1.0	Tau	2.2 ± 0.3	-1.4 ± 0.5	0	3723 ± 125	3.87 ± 0.22	1.36 ± 0.32	8.2 ± 2.0	0.12 ± 0.04
J04162810+2807358	M2.0	Tau	1.1 ± 0.3	-2.7 ± 0.0	1	3713 ± 138	3.85 ± 0.21	<2.26	27.3 ± 2.3	0.23 ± 0.04
J04173372+2820468	M2.3	Tau	0.1 ± 0.5	-1.3 ± 0.1	0	3445 ± 155	3.73 ± 0.28	<1.31	10.8 ± 2.3	0.81 ± 0.13
J04173893+2833005	M2.2	Tau	0.9 ± 0.3	-2.6 ± 0.0	1	3658 ± 136	4.06 ± 0.25	<2.53	34.4 ± 2.6	0.15 ± 0.05
J04174965+2829362	M3.7	Tau	1.4 ± 0.3	-0.8 ± 0.1	0	3315 ± 129	3.37 ± 0.25	1.22 ± 0.33	9.7 ± 2.0	0.28 ± 0.06
J04181078+2519574	M1.0	Tau	-0.7 ± 0.3	-0.7 ± 0.1	0	3721 ± 149	3.67 ± 0.23	<1.12	15.6 ± 2.2	0.32 ± 0.07
J04182909+2826191	M3.5	Tau	⋯	⋯	1	3618 ± 327	4.05 ± 0.59	<2.32	30.7 ± 7.4	0.39 ± 0.20
J04183112+2816290	M3.5	Tau	2.0 ± 0.6	-0.5 ± 0.1	0	3250 ± 207	3.47 ± 0.37	<1.48	16.9 ± 3.1	1.82 ± 0.26
J04183158+2816585	M4.2	Tau	1.3 ± 0.7	0.2 ± 0.2	1	3385 ± 210	3.83 ± 0.35	<1.70	31.4 ± 3.1	0.64 ± 0.12
J04183444+2830302	M0.0	Tau	⋯	⋯	0	4230 ± 142	4.53 ± 0.27	1.84 ± 0.49	10.9 ± 3.0	0.44 ± 0.08
J04184703+2820073	K8.0	Tau	1.8 ± 0.1	-2.6 ± 0.0	1	3806 ± 81	3.69 ± 0.14	2.63 ± 0.27	16.8 ± 1.7	0.26 ± 0.01
J04191281+2829330	M3.5	Tau	1.4 ± 0.4	-1.2 ± 0.2	1	3296 ± 170	3.93 ± 0.30	<1.43	18.9 ± 2.4	0.63 ± 0.10
J04191583+2906269	M0.5	Tau	0.2 ± 0.3	-0.9 ± 0.1	0	3719 ± 130	4.01 ± 0.25	2.19 ± 0.37	9.9 ± 2.3	1.36 ± 0.11
J04192625+2826142	K8.0	Tau	1.1 ± 0.2	-2.2 ± 0.2	0	3830 ± 124	3.91 ± 0.21	2.22 ± 0.30	9.8 ± 2.0	0.20 ± 0.03
J04194127+2749484	M0.0	Tau	0.9 ± 0.2	-2.7 ± 0.0	0	3853 ± 153	4.08 ± 0.26	<1.94	15.6 ± 2.5	0.19 ± 0.05
J04202606+2804089	M3.5	Tau	0.4 ± 0.6	-0.5 ± 0.3	0	3407 ± 197	4.09 ± 0.35	1.37 ± 0.63	10.5 ± 2.8	0.22 ± 0.10
J04214323+1934133	M2.4	Tau	3.5 ± 0.6	-0.5 ± 0.1	2	3543 ± 168	3.27 ± 0.27	1.04 ± 0.35	7.9 ± 2.2	0.70 ± 0.09
J04215563+2755060	M2.3	Tau	0.3 ± 0.5	-0.9 ± 0.1	0	3463 ± 157	3.45 ± 0.27	<1.01	9.4 ± 2.2	1.11 ± 0.11
J04215943+1932063	K0.0	Tau	1.1 ± 0.4	0.0 ± 0.1	0	4065 ± 232	3.51 ± 0.40	<2.34	21.5 ± 4.2	4.90 ± 0.85
J04220217+2657304	M0.0	Tau	2.6 ± 0.3	-0.3 ± 0.2	1	3810 ± 186	4.12 ± 0.36	<2.34	20.8 ± 3.7	1.38 ± 0.19
J04220313+2825389	M2.5	Tau	1.2 ± 0.4	-2.4 ± 0.1	0	3659 ± 226	4.17 ± 0.36	<2.67	43.7 ± 3.8	0.13 ± 0.09
J04221675+2654570	M1.5	Tau	3.7 ± 0.6	-0.8 ± 0.1	0	3586 ± 236	3.83 ± 0.44	2.20 ± 0.77	16.4 ± 3.5	1.74 ± 0.26
J04244457+2610141	M2.8	Tau	4.1 ± 0.7	-0.8 ± 0.0	1	3624 ± 356	4.01 ± 0.64	1.55 ± 0.98	11.1 ± 5.5	2.47 ± 0.63
J04245708+2711565	M0.6	Tau	0.7 ± 0.4	-1.0 ± 0.1	0	3686 ± 183	4.16 ± 0.28	2.46 ± 0.43	11.5 ± 2.5	1.23 ± 0.15
J04265352+2606543	M0.0	Tau	4.7 ± 0.4	⋯	0	4034 ± 182	3.74 ± 0.35	<2.36	37.5 ± 3.2	0.95 ± 0.20
J04265440+2606510	M2.5	Tau	3.5 ± 0.5	-1.1 ± 0.1	0	3456 ± 136	3.53 ± 0.23	<2.01	38.6 ± 2.4	0.33 ± 0.06
J04270469+2606163	K7.0	Tau	2.1 ± 0.4	-0.0 ± 0.1	2	3969 ± 216	3.20 ± 0.28	<1.78	26.9 ± 4.3	4.82 ± 0.94
J04293606+2435556	M3.0	Tau	3.1 ± 0.6	-1.3 ± 0.2	1	3557 ± 172	3.74 ± 0.28	<2.28	24.6 ± 2.7	0.38 ± 0.08
J04294155+2632582	M2.3	Tau	0.3 ± 0.3	-1.0 ± 0.3	0	3477 ± 125	3.89 ± 0.22	2.21 ± 0.32	8.4 ± 2.1	1.24 ± 0.10
J04294247+2632493	M0.7	Tau	0.8 ± 0.2	-1.7 ± 0.4	0	3675 ± 102	3.61 ± 0.17	<1.05	12.2 ± 1.8	0.23 ± 0.03
J04295156+2606448	M1.1	Tau	2.6 ± 0.5	-1.0 ± 0.1	0	3612 ± 176	3.72 ± 0.31	1.81 ± 0.53	14.3 ± 2.5	1.42 ± 0.15
J04300357+1813494	M2.0	Tau	0.6 ± 0.4	-2.7 ± 0.0	0	3527 ± 127	4.07 ± 0.19	2.41 ± 0.32	11.7 ± 2.1	0.02 ± 0.03
J04300399+1813493	K0.0	Tau	1.9 ± 0.2	-1.1 ± 0.4	0	4606 ± 233	4.43 ± 0.42	<1.70	26.0 ± 4.5	1.81 ± 0.44
J04302961+2426450	M2.2	Tau	2.2 ± 0.3	-1.1 ± 0.2	0	3587 ± 114	3.82 ± 0.21	<1.02	8.3 ± 2.0	0.61 ± 0.07
J04304425+2601244	K8.5	Tau	3.2 ± 0.3	-0.9 ± 0.0	1	3809 ± 183	4.00 ± 0.35	2.55 ± 0.64	17.6 ± 3.3	3.16 ± 0.29
J04305137+2442222	M4.3	Tau	0.9 ± 0.4	-1.2 ± 0.1	1	3277 ± 144	3.61 ± 0.27	<1.52	18.4 ± 2.4	0.41 ± 0.08
J04311444+2710179	K8.0	Tau	0.3 ± 0.2	-2.2 ± 0.2	0	3802 ± 139	4.06 ± 0.26	2.01 ± 0.41	13.9 ± 2.4	0.12 ± 0.05
J04312382+2410529	M4.5	Tau	0.9 ± 0.6	-2.6 ± 0.1	1	3203 ± 171	4.14 ± 0.37	<1.55	16.6 ± 3.1	0.92 ± 0.14
J04314007+1813571	M2.0	Tau	-0.1 ± 0.9	-0.3 ± 0.2	2	3606 ± 262	3.24 ± 0.35	<1.87	17.1 ± 3.6	3.85 ± 0.56
J04315056+2424180	M1.0	Tau	2.3 ± 0.6	-0.6 ± 0.3	0	3598 ± 203	3.64 ± 0.35	<1.58	22.9 ± 2.9	0.93 ± 0.14
J04315779+1821350	M3.3	Tau	2.6 ± 0.4	⋯	1	3492 ± 161	3.74 ± 0.29	<1.84	23.0 ± 2.9	0.36 ± 0.09
J04315779+1821380	M1.7	Tau	2.2 ± 0.5	⋯	0	3518 ± 162	3.65 ± 0.26	<1.93	18.2 ± 2.5	0.30 ± 0.07
J04320926+1757227	K6.0	Tau	0.4 ± 0.1	-2.7 ± 0.0	0	4122 ± 96	4.20 ± 0.18	<2.62	30.9 ± 2.1	0.16 ± 0.04
J04321456+1820147	M2.0	Tau	0.7 ± 0.2	-2.7 ± 0.0	1	3610 ± 91	3.91 ± 0.15	<2.42	20.8 ± 1.8	0.13 ± 0.02
J04321885+2422271	M0.8	Tau	2.0 ± 0.4	-2.8 ± 0.1	0	3684 ± 139	3.65 ± 0.22	<1.88	32.1 ± 2.3	0.15 ± 0.05
J04323034+1731406	K7.5	Tau	0.8 ± 0.3	-0.8 ± 0.1	0	3711 ± 121	3.68 ± 0.20	<1.10	10.4 ± 1.9	0.98 ± 0.07
J04323058+2419572	M0.1	Tau	3.2 ± 0.5	-1.2 ± 0.2	0	3925 ± 222	3.90 ± 0.37	1.71 ± 0.76	13.0 ± 3.1	0.78 ± 0.14
J04323176+2420029	M0.5	Tau	3.0 ± 0.8	-0.9 ± 0.1	2	3751 ± 318	3.37 ± 0.48	1.20 ± 0.88	8.2 ± 4.6	5.53 ± 1.05
J04324282+2552314	M2.0	Tau	0.6 ± 0.5	⋯	0	3426 ± 179	3.79 ± 0.33	<1.47	18.6 ± 2.5	0.24 ± 0.10
J04324303+2552311	M1.9	Tau	1.6 ± 1.8	-0.8 ± 0.1	1	3670 ± 437	3.90 ± 0.64	<2.23	31.0 ± 9.7	3.06 ± 0.97
J04324373+1802563	K6.0	Tau	0.4 ± 0.2	-2.7 ± 0.1	0	3912 ± 126	4.11 ± 0.23	1.40 ± 0.35	7.5 ± 2.2	0.12 ± 0.04
J04324911+2253027	K5.5	Tau	3.6 ± 0.6	-0.8 ± 0.2	0	4105 ± 394	4.15 ± 0.64	<2.40	38.2 ± 8.2	1.58 ± 0.59
J04324938+2253082	M4.5	Tau	3.9 ± 0.9	-1.2 ± 0.1	2	3380 ± 247	3.42 ± 0.42	<1.18	18.1 ± 3.4	0.37 ± 0.14

Table 3
(Continued)

2MASS	SpT	Cluster	A_V mag	α_{K_s-W4}	Flag	T K	$\log g$ dex	B kG	$v \sin i$ km s^{-1}	r_K
J04325323+1735337	M2.0	Tau	0.5 ± 0.5	-2.0 ± 0.2	0	3543 ± 132	3.65 ± 0.22	<1.10	11.4 ± 2.0	0.09 ± 0.04
J04330622+2409339	M2.0	Tau	1.0 ± 0.5	-1.1 ± 0.2	0	3553 ± 160	3.64 ± 0.26	<1.59	28.1 ± 2.5	0.57 ± 0.09
J04330664+2409549	K7.0	Tau	1.0 ± 0.3	-1.4 ± 0.2	1	3880 ± 177	4.20 ± 0.35	2.50 ± 0.71	19.9 ± 4.5	1.16 ± 0.15
J04331003+2433433	K7.5	Tau	0.5 ± 0.1	-2.8 ± 0.1	0	3878 ± 80	3.89 ± 0.14	<2.40	31.6 ± 1.8	0.16 ± 0.02
J04333405+2421170	M0.4	Tau	1.9 ± 0.4	-0.7 ± 0.1	0	3689 ± 185	3.79 ± 0.32	1.92 ± 0.44	12.1 ± 2.6	1.42 ± 0.15
J04333456+2421058	K6.5	Tau	1.5 ± 0.3	-0.7 ± 0.1	0	3842 ± 203	3.83 ± 0.33	<2.05	21.2 ± 3.0	1.57 ± 0.18
J04333678+2609492	M0.0	Tau	1.9 ± 0.4	-0.9 ± 0.1	0	3581 ± 152	3.98 ± 0.25	2.28 ± 0.37	11.8 ± 2.4	0.71 ± 0.09
J04333906+2520382	K5.5	Tau	0.9 ± 0.5	-0.8 ± 0.1	0	3930 ± 222	3.80 ± 0.43	1.95 ± 0.70	11.0 ± 3.7	3.23 ± 0.42
J04334871+1810099	M3.0	Tau	0.1 ± 0.3	-0.6 ± 0.5	0	3449 ± 103	4.09 ± 0.18	1.63 ± 0.29	5.7 ± 2.0	0.08 ± 0.03
J04335200+2250301	K5.5	Tau	1.3 ± 0.2	-0.9 ± 0.1	0	3951 ± 94	3.77 ± 0.17	1.95 ± 0.31	12.5 ± 1.9	2.34 ± 0.09
J04335470+2613275	K5.0	Tau	2.6 ± 0.4	-1.2 ± 0.1	0	3977 ± 195	4.09 ± 0.35	<2.83	36.4 ± 3.8	0.71 ± 0.14
J04341099+2251445	M1.5	Tau	1.8 ± 0.5	-2.7 ± 0.0	0	3589 ± 154	3.97 ± 0.26	2.16 ± 0.40	13.3 ± 2.3	0.09 ± 0.06
J04345542+2428531	M0.6	Tau	4.9 ± 0.3	-0.8 ± 0.2	0	3751 ± 171	3.87 ± 0.26	2.16 ± 0.41	12.5 ± 2.3	1.56 ± 0.12
J04352020+2232146	M3.2	Tau	0.5 ± 0.7	-1.1 ± 0.1	0	3493 ± 240	4.00 ± 0.48	<1.62	20.2 ± 3.8	1.04 ± 0.22
J04352089+2254242	K8.0	Tau	1.9 ± 0.4	-2.8 ± 0.1	0	3856 ± 195	3.87 ± 0.30	<0.90	6.2 ± 2.4	0.17 ± 0.06
J04352450+1751429	M2.6	Tau	0.9 ± 0.4	-2.6 ± 0.0	1	3494 ± 146	4.28 ± 0.21	2.44 ± 0.33	5.0 ± 2.3	0.04 ± 0.04
J04352737+2414589	M0.3	Tau	0.1 ± 0.4	-0.9 ± 0.2	0	3648 ± 144	3.74 ± 0.22	1.54 ± 0.37	10.9 ± 2.1	0.43 ± 0.05
J04354093+2411087	M0.5	Tau	4.6 ± 0.4	-1.0 ± 0.0	0	3665 ± 154	3.85 ± 0.26	2.33 ± 0.34	8.2 ± 2.1	0.77 ± 0.08
J04354733+2250216	K2.0	Tau	2.4 ± 0.3	-0.7 ± 0.1	0	4265 ± 255	4.22 ± 0.44	<2.85	43.0 ± 5.0	1.18 ± 0.32
J04355277+2254231	K4.0	Tau	3.0 ± 0.5	-0.6 ± 0.2	1	4096 ± 380	4.07 ± 0.62	<1.79	18.6 ± 8.8	2.23 ± 0.90
J04355349+2254089	M0.6	Tau	2.3 ± 0.3	⋯	0	3760 ± 164	3.84 ± 0.26	<2.65	43.3 ± 2.9	0.25 ± 0.07
J04355684+2254360	M2.0	Tau	2.0 ± 0.6	-0.9 ± 0.1	0	3406 ± 207	3.99 ± 0.43	<1.22	12.5 ± 3.1	0.88 ± 0.20
J04355892+2238353	K8.0	Tau	0.9 ± 0.3	-2.7 ± 0.1	0	3869 ± 169	4.10 ± 0.29	<2.54	29.1 ± 3.5	0.16 ± 0.07
J04361909+2542589	K5.0	Tau	0.3 ± 0.2	-2.9 ± 0.1	0	4134 ± 126	4.07 ± 0.24	<1.72	22.8 ± 2.5	0.15 ± 0.07
J04382858+2610494	M0.3	Tau	1.3 ± 0.6	-0.5 ± 0.1	2	3704 ± 350	3.44 ± 0.50	1.78 ± 0.85	12.7 ± 5.4	5.44 ± 1.04
J04390163+2336029	M4.9	Tau	0.1 ± 0.5	-1.3 ± 0.1	1	3221 ± 188	3.86 ± 0.36	<1.27	17.8 ± 2.7	0.52 ± 0.12
J04391779+2221034	K5.5	Tau	0.8 ± 0.2	-1.1 ± 0.2	0	4156 ± 123	4.11 ± 0.23	<1.83	15.4 ± 2.3	1.08 ± 0.10
J04392090+2545021	M2.5	Tau	3.9 ± 0.4	-1.0 ± 0.1	0	3536 ± 152	3.76 ± 0.28	<1.58	13.8 ± 2.4	1.47 ± 0.15
J04400800+2605253		Tau	7.2 ± 0.5	-0.6 ± 0.1	0	3749 ± 273	3.84 ± 0.49	2.32 ± 0.97	16.6 ± 4.3	1.52 ± 0.28
J04410470+2451062	M0.9	Tau	0.7 ± 0.2	-2.7 ± 0.0	0	3663 ± 115	4.07 ± 0.19	2.28 ± 0.29	8.3 ± 2.0	0.10 ± 0.04
J04411681+2840000	M1.1	Tau	2.4 ± 0.3	-0.6 ± 0.6	0	3706 ± 121	3.70 ± 0.21	<1.90	26.3 ± 2.2	0.22 ± 0.04
J04413882+2556267	M0.0	Tau	3.3 ± 0.3	-0.1 ± 0.1	0	3738 ± 161	3.74 ± 0.26	<1.80	24.2 ± 2.6	0.59 ± 0.09
J04420548+2522562	M0.5	Tau	3.0 ± 0.3	-2.2 ± 0.1	0	3779 ± 146	3.89 ± 0.24	<2.22	21.7 ± 2.6	0.25 ± 0.05
J04420777+2523118	K7.0	Tau	3.0 ± 0.3	⋯	0	3763 ± 160	3.93 ± 0.28	1.59 ± 0.49	11.0 ± 2.5	1.40 ± 0.12
J04423769+2515374	M0.8	Tau	0.7 ± 0.5	-0.3 ± 0.1	0	3758 ± 282	3.91 ± 0.43	<1.89	19.9 ± 4.1	1.60 ± 0.25
J04430309+2520187	M2.3	Tau	1.0 ± 0.6	-0.9 ± 0.2	0	3487 ± 181	3.89 ± 0.31	<1.30	12.3 ± 2.5	0.49 ± 0.11
J04465305+1700001	M0.6	Tau	1.3 ± 0.8	-0.7 ± 0.1	1	3704 ± 319	3.88 ± 0.57	<1.86	17.7 ± 4.9	0.59 ± 0.23
J04465897+1702381	K8.0	Tau	2.4 ± 0.4	-1.1 ± 0.1	0	3903 ± 243	3.53 ± 0.35	<1.30	12.8 ± 3.1	2.36 ± 0.36
J04474859+2925112	M0.4	Tau	0.9 ± 0.2	-1.2 ± 0.1	0	3879 ± 138	3.89 ± 0.25	2.09 ± 0.41	13.4 ± 2.3	1.79 ± 0.13
J04514737+3047134	K7.0	Tau	0.8 ± 0.6	-0.2 ± 0.0	0	3780 ± 279	3.79 ± 0.49	<1.80	21.4 ± 4.3	3.03 ± 0.45
J04551098+3021595	K6.0	Tau	0.9 ± 0.3	-0.6 ± 0.5	0	4020 ± 99	4.02 ± 0.19	2.11 ± 0.34	14.4 ± 2.0	0.48 ± 0.05
J04553695+3017553	K2.0	Tau	-0.1 ± 0.1	-2.5 ± 0.1	0	4450 ± 122	4.26 ± 0.25	<1.95	21.8 ± 2.8	0.24 ± 0.09
J04560201+3021037	K6.0	Tau	0.6 ± 0.3	-2.4 ± 0.1	0	4034 ± 100	3.99 ± 0.19	<1.61	14.2 ± 2.0	0.18 ± 0.04
J05030659+2523197	M0.8	Tau	1.1 ± 0.2	-1.0 ± 0.2	1	3760 ± 158	4.01 ± 0.26	2.67 ± 0.40	11.8 ± 2.4	0.68 ± 0.08
J05071206+2437163	K6.0	Tau	0.5 ± 0.3	-2.6 ± 0.0	0	3987 ± 131	4.11 ± 0.25	<2.00	21.6 ± 2.5	0.09 ± 0.05
J05074953+3024050	K2.0	Tau	3.4 ± 0.7	-0.8 ± 0.1	0	3885 ± 215	4.10 ± 0.39	<2.02	16.6 ± 3.9	2.09 ± 0.29
J10120908-3124451	M4.0	TWA	1.1 ± 0.2	-1.6 ± 0.1	1	3315 ± 87	4.06 ± 0.18	<1.34	18.0 ± 2.0	0.28 ± 0.03
J10423011-3340162	M3.2	TWA	⋯	⋯	0	3327 ± 80	4.27 ± 0.13	2.19 ± 0.26	7.4 ± 1.7	0.10 ± 0.00
J11015191-3442170	M0.5	TWA	⋯	⋯	0	3783 ± 107	4.35 ± 0.18	2.75 ± 0.30	8.4 ± 2.0	0.53 ± 0.05
J11091380-3001398	M2.2	TWA	⋯	⋯	0	3557 ± 92	4.07 ± 0.16	<1.38	15.9 ± 1.9	0.06 ± 0.02
J11102788-3731520	M4.1	TWA	⋯	⋯	1	3284 ± 75	4.00 ± 0.13	<0.97	11.9 ± 1.7	0.29 ± 0.00
J11210549-3845163	M2.75	TWA	⋯	⋯	0	3534 ± 104	4.19 ± 0.17	2.67 ± 0.32	19.7 ± 2.0	0.02 ± 0.02
J11211723-3446454	M1.1	TWA	⋯	⋯	0	3638 ± 95	4.14 ± 0.16	2.12 ± 0.29	14.2 ± 1.9	0.04 ± 0.02
J11211745-3446497	M1.0	TWA	⋯	⋯	0	3672 ± 93	4.13 ± 0.16	<1.71	13.7 ± 1.9	0.04 ± 0.02
J11220530-2446393	K6.0	TWA	⋯	⋯	0	4257 ± 102	4.51 ± 0.21	<1.10	10.2 ± 2.1	0.31 ± 0.04
J11324124-2651559	M2.9	TWA	⋯	⋯	0	3397 ± 75	4.30 ± 0.13	2.86 ± 0.26	7.5 ± 1.7	0.13 ± 0.00
J11482373-3728485	M3.4	TWA	0.2 ± 0.2	-2.7 ± 0.1	0	3351 ± 75	4.30 ± 0.14	<1.30	10.9 ± 1.7	0.09 ± 0.00
J11482422-3728491	K6.0	TWA	0.1 ± 0.3	-2.7 ± 0.0	0	4043 ± 94	4.32 ± 0.17	2.29 ± 0.30	12.0 ± 2.0	0.17 ± 0.03
J12072738-3247002	M3.5	TWA	⋯	⋯	1	3404 ± 101	4.15 ± 0.18	<1.42	19.1 ± 1.9	0.16 ± 0.03
J12153072-3948426	M0.5	TWA	⋯	⋯	0	3707 ± 99	4.14 ± 0.17	2.21 ± 0.29	15.0 ± 1.9	0.06 ± 0.03
J12345629-4538075	M3.0	TWA	0.0 ± 0.4	-2.7 ± 0.0	0	3445 ± 90	4.15 ± 0.16	1.85 ± 0.28	12.4 ± 1.9	0.07 ± 0.02
J12350424-4136385	M3.0	TWA	⋯	⋯	1	3357 ± 75	4.23 ± 0.13	2.54 ± 0.26	9.5 ± 1.7	0.10 ± 0.00
J12354893-3950245	M4.5	TWA	0.9 ± 0.4	-2.5 ± 0.0	1	3391 ± 122	4.45 ± 0.22	<1.98	22.8 ± 2.3	0.36 ± 0.04
J12360055-3952156	M2.5	TWA	⋯	⋯	0	3531 ± 115	4.22 ± 0.18	2.23 ± 0.34	14.8 ± 2.1	0.02 ± 0.02

Table 3
(Continued)

2MASS	SpT	Cluster	A_V mag	α_{K_s-W4}	Flag	T K	$\log g$ dex	B kG	$v \sin i$ km s^{-1}	r_K
TWA 3B	M4.0	TWA	⋯	⋯	1	3355 ± 75	4.20 ± 0.13	<1.78	15.8 ± 1.7	0.16 ± 0.00

Note. Columns 1–3 provide target names, spectral types, and membership information. Columns 4 and 5 are the values of the visual extinction and the infrared index computed in this work. Finally, Columns 6–11 present the quality flag, T, $\log g$, B field, $v \sin i$, and K-band veiling determined in Paper I.

(This table is available in machine-readable form.)

Table 4
Stellar Parameters of the K and M Field Stars

Name	SpT	Flag	T	$\log g$	B	$v \sin i$
[RSP2011] 315	⋯	0	3558 ± 186	4.84 ± 0.31	<0.42	4.7 ± 2.9
G 43-43	⋯	0	3655 ± 144	4.90 ± 0.27	<0.32	4.0 ± 2.5
LP 611-70	⋯	0	3494 ± 149	4.24 ± 0.20	<0.42	3.4 ± 2.0
UCAC4 545-148763	⋯	0	3793 ± 140	4.59 ± 0.22	1.45 ± 0.39	5.5 ± 2.7
G 194-18	⋯	2	3748 ± 126	5.32 ± 0.25	<0.40	4.9 ± 3.5
HD 285482	K0.0	0	4744 ± 91	4.63 ± 0.17	<0.34	3.9 ± 2.0
HD 285690	K0.0	0	4843 ± 96	4.61 ± 0.19	<0.33	4.3 ± 2.2
HD 285876	K0.0	0	4190 ± 111	4.58 ± 0.19	<0.26	3.4 ± 2.1
HD 286363	K0.0	0	4606 ± 93	4.54 ± 0.20	<0.36	4.5 ± 2.1
BD+45 598	K0.0	2	4924 ± 111	4.12 ± 0.37	<0.63	22.5 ± 3.6
HD 182488	K0.0	2	4983 ± 78	4.09 ± 0.22	<0.24	4.6 ± 2.1
* 54 Psc	K0.5	2	4993 ± 75	4.27 ± 0.15	<0.09	3.4 ± 1.8
* 107 Psc	K1.0	2	4996 ± 75	4.25 ± 0.15	<0.05	5.0 ± 1.8
HD 125455	K1.0	2	4990 ± 76	4.10 ± 0.18	<0.13	4.8 ± 1.9
HD 285348	K2.0	0	4637 ± 90	4.56 ± 0.18	<0.37	3.3 ± 2.1
HD 3765	K2.0	0	4815 ± 80	4.28 ± 0.15	<0.09	2.3 ± 1.7
BD+20 2720	K2.0	2	4980 ± 79	3.31 ± 0.24	<0.15	3.9 ± 2.0
HD 21845	K2.0	2	4957 ± 99	4.36 ± 0.28	<0.52	18.4 ± 2.9
HD 220339	K2.0	2	4936 ± 128	3.98 ± 0.46	<0.59	8.4 ± 4.4
HD 88925	K2.0	2	4992 ± 75	3.14 ± 0.19	<0.06	5.4 ± 1.8
HD 122064	K3.0	0	4554 ± 77	4.24 ± 0.14	<0.08	2.5 ± 1.7
HD 219134	K3.0	0	4687 ± 90	4.34 ± 0.18	<0.18	3.0 ± 1.9
HD 52919	K4.0	2	4616 ± 91	4.48 ± 0.21	<0.21	2.9 ± 2.0
BD+49 2125	K4/5	1	4535 ± 130	4.36 ± 0.30	<0.82	12.0 ± 2.6
BD-09 2926B	K5	1	4584 ± 106	4.61 ± 0.25	<0.28	4.0 ± 2.3
BD+20 1790	K5.0	0	4352 ± 335	4.77 ± 0.22	2.61 ± 0.49	10.8 ± 2.3
HD 286554	K5.0	0	4067 ± 117	4.51 ± 0.18	<0.28	3.3 ± 2.0
BD-09 4191	K5.0	1	3719 ± 150	5.16 ± 0.30	<0.39	7.8 ± 3.6
HD 98800	K5.0	1	4340 ± 90	4.20 ± 0.18	<0.59	10.3 ± 2.0
HD 122120	K5.0	2	4369 ± 86	4.32 ± 0.16	<0.18	2.6 ± 1.8
BD+05 378	K6.0	0	4144 ± 290	4.67 ± 0.41	2.27 ± 0.72	12.1 ± 3.3
HD 88230	K6.0	0	3843 ± 104	4.31 ± 0.16	<0.26	3.2 ± 2.0
HD 283869	K7.0	0	4369 ± 83	4.28 ± 0.15	<0.15	2.7 ± 1.8
HD 6440B	K7.0	0	3854 ± 97	4.77 ± 0.16	<0.17	3.3 ± 1.9
LP 533-57	K7.0	0	3873 ± 83	4.36 ± 0.15	<0.29	4.5 ± 1.9
HD 21845B	K7.0	1	3758 ± 198	4.53 ± 0.35	<2.72	26.8 ± 4.6
HD 157881	K7.0	2	3877 ± 80	4.37 ± 0.14	<0.29	2.5 ± 1.8
HD 97101	K7.0	2	3874 ± 80	4.25 ± 0.14	<0.13	2.5 ± 1.8
BD+06 2986	K8.0	1	3846 ± 88	5.09 ± 0.16	<0.12	3.1 ± 1.9
BD-13 6424	M0.0	0	3682 ± 176	4.49 ± 0.26	1.96 ± 0.41	9.1 ± 2.8
BD+02 1729	M0.0	0	3743 ± 91	4.44 ± 0.15	<0.28	3.6 ± 1.9
BD+13 2618	M0.0	0	3631 ± 102	4.37 ± 0.16	2.21 ± 0.29	12.5 ± 1.9
BD+23 2063B	M0.0	0	3749 ± 142	4.23 ± 0.21	<0.43	3.7 ± 2.2
BD+33 1505	M0.0	0	3692 ± 117	4.58 ± 0.18	<0.37	3.5 ± 2.0
BD+36 2322	M0.0	0	3732 ± 123	4.73 ± 0.21	2.22 ± 0.36	12.8 ± 2.4
HD 19305	M0.0	0	3860 ± 80	4.54 ± 0.14	<0.15	2.6 ± 1.8
HD 79211	M0.0	0	3759 ± 128	4.66 ± 0.19	<0.23	3.1 ± 2.0
HIP 17248	M0.0	0	3754 ± 194	4.54 ± 0.25	2.24 ± 0.43	5.4 ± 2.8
Ross 1050	M0.0	0	3793 ± 125	5.10 ± 0.24	<0.28	4.7 ± 2.7
StKM 1-82	M0.0	0	3816 ± 126	4.76 ± 0.21	<0.49	5.1 ± 2.4
TYC 5174-242-1	M0.0	0	3749 ± 137	4.69 ± 0.24	<0.68	9.9 ± 2.6
BD+30 397B	M0.0	1	3563 ± 147	4.74 ± 0.24	2.84 ± 0.37	8.1 ± 2.3

Table 4
(Continued)

Name	SpT	Flag	T	$\log g$	B	$v \sin i$
CCDM J10095+4126AB	M0.0	1	4768 ± 115	4.71 ± 0.24	<0.89	9.6 ± 2.6
GSC 04686-00596	M0.0	1	4001 ± 210	4.53 ± 0.31	<2.87	37.9 ± 3.8
HD 59438C	M0.0	1	3821 ± 120	5.26 ± 0.26	<0.26	10.8 ± 3.1
StKM 1-516	M0.0	1	3826 ± 102	5.16 ± 0.18	<0.13	3.6 ± 2.1
HD 209290	M0.5	0	3662 ± 100	4.55 ± 0.16	<0.32	2.8 ± 1.9
HD 28343	M0.5	0	3821 ± 96	4.19 ± 0.15	<0.31	3.0 ± 1.9
GJ 3653	M0.5	1	3794 ± 145	4.77 ± 0.29	<2.18	34.6 ± 3.8
MCC 124	M0.7	1	3847 ± 104	5.16 ± 0.20	1.60 ± 0.53	9.2 ± 3.0
2MASS J14040922+2044314	M1.0	0	3655 ± 141	4.78 ± 0.24	<0.78	5.3 ± 2.5
BD+61 1678C	M1.0	0	3627 ± 123	4.62 ± 0.19	<0.34	3.6 ± 2.1
HD 199305	M1.0	0	3600 ± 88	4.60 ± 0.15	<0.21	2.5 ± 1.8
HD 42581	M1.0	0	3589 ± 147	4.50 ± 0.21	<0.40	3.5 ± 2.2
LP 353-51	M1.0	0	3772 ± 115	4.79 ± 0.18	1.59 ± 0.32	4.0 ± 2.2
BD+02 348	M1.0	1	3882 ± 77	5.46 ± 0.14	<0.07	3.3 ± 1.9
HD 263175B	M1.0	1	3845 ± 102	5.35 ± 0.20	<0.21	4.0 ± 2.4
BD+44 2051	M1.0	2	3872 ± 81	5.47 ± 0.14	<0.10	3.4 ± 2.0
2MASS J00393579-3816584	M1.4	1	3535 ± 116	4.55 ± 0.17	2.54 ± 0.32	9.0 ± 1.9
* tet Per B	M1.5	0	3584 ± 96	4.76 ± 0.16	<0.25	2.8 ± 1.9
BD+18 3421	M1.5	0	3856 ± 108	5.38 ± 0.18	<0.07	5.5 ± 1.9
HD 31867B	M1.5	0	3589 ± 182	4.71 ± 0.30	<0.36	4.5 ± 2.8
LP 298-53	M1.5	0	3622 ± 159	4.92 ± 0.26	1.77 ± 0.39	6.1 ± 2.6
NLTT 19115	M1.5	0	3703 ± 130	5.01 ± 0.21	<0.24	3.7 ± 2.2
Wolf 58	M1.5	0	3648 ± 153	4.69 ± 0.22	1.82 ± 0.35	6.8 ± 2.4
HD 154363B	M1.5	1	3771 ± 108	5.13 ± 0.21	<0.12	3.6 ± 2.1
G 202-48	M1.5	2	3852 ± 94	5.46 ± 0.14	<0.15	5.1 ± 2.3
LP 493-31	M1.5	2	3591 ± 129	5.12 ± 0.21	<0.18	3.2 ± 2.2
BD+01 2447	M2.0	0	3684 ± 95	5.11 ± 0.17	<0.12	3.6 ± 1.9
BD+25 3173	M2.0	0	3599 ± 108	4.73 ± 0.18	<0.21	3.2 ± 1.9
BD+44 3567	M2.0	0	3716 ± 109	5.14 ± 0.19	<0.16	3.5 ± 2.1
HD 119850	M2.0	0	3693 ± 87	5.06 ± 0.16	<0.06	3.3 ± 1.8
HD 217987	M2.0	0	3742 ± 121	5.13 ± 0.21	<0.21	3.8 ± 2.2
V* AN Sex	M2.0	0	3550 ± 124	4.67 ± 0.20	<0.32	3.3 ± 2.1
Ross 799	M2.0	1	3476 ± 156	4.61 ± 0.26	<0.36	4.0 ± 2.4
HD 349726	M2.0	2	3876 ± 80	5.46 ± 0.14	<0.09	3.9 ± 2.1
Ross 730	M2.0	2	3875 ± 80	5.47 ± 0.14	<0.08	3.1 ± 1.9
* 18 Pup B	M2.5	0	3585 ± 156	4.87 ± 0.28	<0.32	5.2 ± 2.6
* tau Cyg C	M2.5	0	3696 ± 144	5.16 ± 0.26	<0.35	4.7 ± 2.8
G 145-11	M2.5	0	3686 ± 166	4.98 ± 0.31	<0.38	4.7 ± 3.1
HD 285968	M2.5	0	3477 ± 128	4.64 ± 0.20	<0.36	3.5 ± 2.2
HD 38529B	M2.5	0	3404 ± 178	4.47 ± 0.27	<0.39	3.9 ± 2.4
HD 50281B	M2.5	0	3633 ± 109	5.00 ± 0.18	<0.26	3.5 ± 2.1
Ross 265	M2.5	0	3512 ± 112	4.67 ± 0.21	<0.41	8.3 ± 2.0
UCAC4 315-070111	M2.5	0	3634 ± 116	5.15 ± 0.21	2.14 ± 0.38	9.6 ± 2.4
G 155-29	M2.5	1	3633 ± 129	4.99 ± 0.23	<0.17	6.2 ± 2.2
LP 222-50	M2.5	2	3776 ± 115	5.35 ± 0.21	<0.22	3.8 ± 2.3
LP 636-19	M2.9	1	3554 ± 124	4.94 ± 0.26	<0.71	15.0 ± 2.5
G 121-42	M3.0	0	3681 ± 106	5.12 ± 0.19	<0.10	3.8 ± 2.0
GJ 752	M3.0	0	3492 ± 99	4.68 ± 0.18	<0.21	3.3 ± 1.9
GJ569	M3.0	0	3651 ± 129	4.99 ± 0.22	<0.99	5.1 ± 2.5
Ross 905	M3.0	0	3569 ± 107	4.91 ± 0.18	<0.14	3.2 ± 1.9
BD+68 946	M3.0	1	3600 ± 99	4.99 ± 0.17	<0.10	3.3 ± 2.0
G 80-21	M3.0	1	3603 ± 210	4.92 ± 0.36	2.51 ± 0.79	9.2 ± 5.6
HD 173739	M3.0	1	3878 ± 79	5.48 ± 0.13	<0.06	2.8 ± 1.8
UCAC4 595-047332	M3.0	1	3675 ± 149	5.26 ± 0.26	1.67 ± 0.55	7.0 ± 3.3
G 83-44	M3.45	0	3494 ± 116	4.77 ± 0.21	<0.19	3.5 ± 2.1
* ksi Peg B	M3.5	0	3749 ± 139	5.23 ± 0.26	<0.31	5.0 ± 2.9
BD+05 1668	M3.5	1	3746 ± 109	5.32 ± 0.19	<0.06	3.5 ± 1.9
CD-44 11909	M3.5	1	3433 ± 107	4.94 ± 0.22	<0.15	7.1 ± 2.0
HD 127871B	M3.5	1	3713 ± 154	5.24 ± 0.26	<0.24	4.6 ± 2.7
BD-15 6290	M3.5	2	3467 ± 101	5.06 ± 0.18	<0.16	2.7 ± 1.9
G 106-36	M3.5	2	3680 ± 152	5.28 ± 0.29	<0.31	6.7 ± 2.9
HD 173740	M3.5	2	3882 ± 78	5.49 ± 0.13	<0.06	4.5 ± 2.1
V* CW UMa	M3.5	2	3812 ± 124	5.39 ± 0.19	3.60 ± 0.49	5.2 ± 3.5
Wolf 1062	M3.5	2	3883 ± 78	5.48 ± 0.13	<0.04	6.9 ± 1.8

Table 4
(Continued)

Name	SpT	Flag	T	$\log g$	B	$v \sin i$
Ross 104	M4.0	0	3648 ± 97	5.10 ± 0.18	<0.17	3.7 ± 2.0
BD+20 2465	M4.0	1	3548 ± 91	5.11 ± 0.17	2.55 ± 0.33	2.9 ± 1.9
G 96-10	M4.0	1	3603 ± 128	5.25 ± 0.24	<0.35	3.6 ± 2.3
HD 18143C	M4.0	1	3515 ± 188	4.93 ± 0.36	<0.48	4.9 ± 3.2
LP 642-48	M4.0	1	3614 ± 137	5.21 ± 0.24	3.44 ± 0.36	14.2 ± 2.3
Ross 689	M4.0	1	3570 ± 125	5.05 ± 0.21	<0.18	3.6 ± 2.2
UCAC4 468-040412	M4.0	1	3575 ± 152	5.21 ± 0.24	<0.33	4.0 ± 2.4
V* WW PsA	M4.0	1	3578 ± 131	4.89 ± 0.26	2.39 ± 0.53	16.1 ± 2.6
V* YZ CMi	M4.0	1	3606 ± 111	5.36 ± 0.18	3.81 ± 0.29	3.3 ± 2.0
Wolf 358	M4.0	1	3463 ± 111	5.05 ± 0.20	<0.16	3.4 ± 2.1
Wolf 414	M4.0	1	3493 ± 106	4.95 ± 0.22	<0.13	8.0 ± 2.0
UCAC4 536-150368	M4.0	2	3798 ± 130	5.43 ± 0.22	2.22 ± 2.07	15.6 ± 5.5
2MASS J23263962+4521141	M4.5	0	3766 ± 149	4.95 ± 0.32	<0.62	9.5 ± 4.1
* rho01 Cnc B	M4.5	2	3391 ± 108	4.89 ± 0.21	<0.14	2.8 ± 1.9
2MASS J04324938+2253082	M4.6	1	3415 ± 271	4.07 ± 0.45	<0.42	20.6 ± 3.6
V* TX PsA	M5.0	1	3720 ± 187	5.04 ± 0.36	<0.33	27.2 ± 2.7
LP 214-42	M5.0	2	3696 ± 229	5.13 ± 0.49	<1.07	45.7 ± 4.7

Note. The stellar parameters are determined using the same MCMC approach, but ignoring K-band veiling. The spectral type references are those indicated in López-Valdivia et al. (2019).

(This table is available in machine-readable form.)

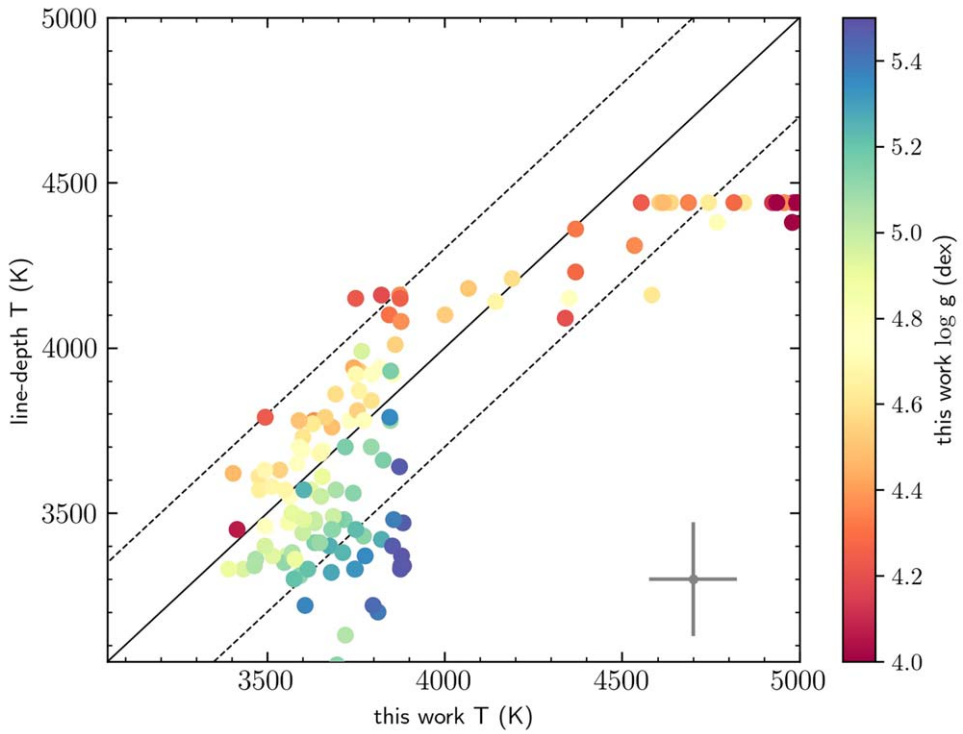

Figure 8. Comparison between our T values and the line-depth temperatures of López-Valdivia et al. (2019) for 133 field stars, color coded by our $\log g$ determinations. The dashed lines denote ± 300 K from the one-to-one relation (solid line). About 73% of the sample is within ± 300 K, but the differences could be as high as 600 K. The error bar in the right corner represents the mean errors of each method, which are of ∼120 and ∼170 K, for this work and the line-depth methods, respectively.

the MCMC analysis. (ii) We extended the synthetic spectral grid to include $\log g$ values up to 5.5 dex, as M field stars might have $\log g$ values close to or even higher than 5.0 dex (e.g., Ségransan et al. 2003). The MARCS library has models with $\log g$ equal to 5.5 dex for T lower than 3900 K. We extended the synthetic grid for T colder than 3900 K.

As with the YSOs, we classified the stellar parameter determination of the field stars with the same quality flag as the YSOs. We assigned a flag equal to 0, 1, 2, or 3 if the determination is good, acceptable, at the edge of our grid, or poor. We found that almost 36% of our field stars (74 of 207) have poor determinations. The reason for this high number is

not clear. We identified some common issues in the stellar spectra that prevented our MCMC analysis from converging into a good fit. We identify some stars with very high $v \sin i$, narrow atomic or molecular lines, and some double lines. The remaining 133 stars, reported in Table 4, are considered our field sample, and we used them throughout the paper.

In Figure 8, we compared the T values determined in here with those values reported by López-Valdivia et al. (2019), color coded by our $\log g$ values. There is an acceptable agreement between the two studies, but we found a trend with our $\log g$ values. The line-depth temperatures are hotter than our values for objects with $\log g \lesssim 4.8$ dex, while the opposite behavior occurs if the $\log g$ that we determined is greater than 4.8 dex. Such trend might be the result of two main things: (i) López-Valdivia et al. (2019) used a different set of synthetic spectra (BT-Settl models), and (ii) they fixed the $\log g$ value to 4.5 dex in their determination method for all the sample. Although this, the majority of our determinations (97 of 133) are within ± 300 K; however, the differences could be as high as 600 K, especially in those objects that have $\log g$ values significantly different from the fixed 4.5 dex used in López-Valdivia et al. (2019). We also see that the line-depth temperatures piled up about $\sim$4400 K, where the method loses its effectiveness in determining temperature.

It is important to mention that we selected and fine-tuned the method, synthetic spectra, line list, and the spectral regions used in this paper to determine the stellar parameters of YSOs, which may not work properly for more evolved stars. Despite this, our stellar parameters follow the theoretical predictions for K and M stars.

ORCID iDs

Ricardo López-Valdivia https://orcid.org/0000-0002-7795-0018
Gregory N. Mace https://orcid.org/0000-0001-7875-6391
Eunkyu Han https://orcid.org/0000-0001-9797-0019
Erica Sawczynec https://orcid.org/0000-0002-8378-1062
Jesús Hernández https://orcid.org/0000-0001-9797-5661
L. Prato https://orcid.org/0000-0001-7998-226X
Christopher M. Johns-Krull https://orcid.org/0000-0002-8828-6386
Heeyoung Oh https://orcid.org/0000-0002-0418-5335
Jae-Joon Lee https://orcid.org/0000-0003-0894-7824
Adam Kraus https://orcid.org/0000-0001-9811-568X
Joe Llama https://orcid.org/0000-0003-4450-0368
Daniel T. Jaffe https://orcid.org/0000-0003-3577-3540

References

Allard, F., Homeier, D., Freytag, B., et al. 2013, MSAIS, 24, 128
Anderson, G. M. 1976, GeCoA, 40, 1533
Baraffe, I., Homeier, D., Allard, F., & Chabrier, G. 2015, A&A, 577, A42
Barenfeld, S. A., Carpenter, J. M., Sargent, A. I., et al. 2019, ApJ, 878, 45
Bean, J. L., Sneden, C., Hauschildt, P. H., Johns-Krull, C. M., & Benedict, G. F. 2006, ApJ, 652, 1604
Cieza, L. A., Schreiber, M. R., Romero, G. A., et al. 2010, ApJ, 712, 925
Cutri, R. M., Skrutskie, M. F., van Dyk, S., et al. 2003, VizieR Online Data Catalog, II/246
Cutri, R. M., Wright, E. L., Conrow, T., et al. 2021, VizieR Online Data Catalog, II/328
Deen, C. P. 2013, AJ, 146, 51
D'Orazi, V., Biazzo, K., & Randich, S. 2011, A&A, 526, A103
Duchêne, G. 2010, ApJL, 709, L114
Dunham, M. M., Allen, L. E., Evans, N. J. I., et al. 2015, ApJS, 220, 11
Elias, J. H. 1978, ApJ, 224, 453
Esplin, T. L., & Luhman, K. L. 2020, AJ, 159, 282
Feiden, G. A. 2016, A&A, 593, A99
Flores, C., Connelley, M. S., Reipurth, B., & Boogert, A. 2019, ApJ, 882, 75
Foreman-Mackey, D., Hogg, D. W., Lang, D., & Goodman, J. 2013, PASP, 125, 306
Gray, D. F. 2005, The Observation and Analysis of Stellar Photospheres (Cambridge: Cambridge Univ. Press)
Großschedl, J. E., Alves, J., Teixeira, P. S., et al. 2019, A&A, 622, A149
Gully-Santiago, M., Wang, W., Deen, C., et al. 2010, Proc. SPIE, 7739, 77393S
Gustafsson, B., Edvardsson, B., Eriksson, K., et al. 2008, A&A, 486, 951
Haisch, K. E. J., Barsony, M., Greene, T. P., & Ressler, M. E. 2002, AJ, 124, 2841
Herczeg, G. J., & Hillenbrand, L. A. 2014, ApJ, 786, 97
Hsieh, T.-H., & Lai, S.-P. 2013, ApJS, 205, 5
Hussaini, M., Mace, G. N., López-Valdivia, R., Honaker, E. J., & Han, E. 2020, RNAAS, 4, 241
Indebetouw, R., Mathis, J. S., Babler, B. L., et al. 2005, ApJ, 619, 931
Jaffe, D. T., Keller, L. D., & Ershov, O. A. 1998, Proc. SPIE, 3354, 201
Johns-Krull, C. M., Valenti, J. A., & Koresko, C. 1999, ApJ, 516, 900
Joy, A. H. 1949, ApJ, 110, 424
Kidder, B., Mace, G., López-Valdivia, R., et al. 2021, ApJ, 922, 27
Kraus, A. L., Ireland, M. J., Martinache, F., & Lloyd, J. P. 2008, ApJ, 679, 762
Lada, C. J., & Wilking, B. A. 1984, ApJ, 287, 610
Lafreniére, D., Jayawardhana, R., van Kerkwijk, M. H., Brandeker, A., & Janson, M. 2014, ApJ, 785, 47
Lavail, A., Kochukhov, O., Hussain, G. A. J., et al. 2017, A&A, 608, A77
Lavail, A., Kochukhov, O., & Hussain, G. A. J. 2019, A&A, 630, A99
Lee, J.-J., Gullikson, K., & Kaplan, K. 2017, igrins/plp v2.2.0, Zenodo, doi:10.5281/zenodo.845059
López-Valdivia, R., Mace, G. N., Sokal, K. R., et al. 2019, ApJ, 879, 105
López-Valdivia, R., Sokal, K. R., Mace, G. N., et al. 2021, ApJ, 921, 53
Luhman, K. L., Allen, P. R., Espaillat, C., Hartmann, L., & Calvet, N. 2010, ApJS, 186, 111
Luhman, K. L., & Esplin, T. L. 2020, AJ, 160, 44
Luhman, K. L., Herrmann, K. A., Mamajek, E. E., Esplin, T. L., & Pecaut, M. J. 2018, AJ, 156, 76
Luhman, K. L., Mamajek, E. E., Shukla, S. J., & Loutrel, N. P. 2017, AJ, 153, 46
Luhman, K. L., Stauffer, J. R., Muench, A. A., et al. 2003, ApJ, 593, 1093
Mace, G., Kim, H., Jaffe, D. T., et al. 2016, Proc. SPIE, 9908, 99080C
Mace, G., Sokal, K., Lee, J.-J., et al. 2018, Proc. SPIE, 10702, 107020Q
Marigo, P., Girardi, L., Bressan, A., et al. 2017, ApJ, 835, 77
Moss, D. 2003, A&A, 403, 693
Park, C., Jaffe, D. T., Yuk, I.-S., et al. 2014, Proc. SPIE, 9147, 91471D
Pecaut, M. J., & Mamajek, E. E. 2013, ApJS, 208, 9
Prato, L. 2007, ApJ, 657, 338
Prato, L., Greene, T. P., & Simon, M. 2003, ApJ, 584, 853
Ratzka, T., Köhler, R., & Leinert, C. 2005, A&A, 437, 611
Rebull, L. M., Stauffer, J. R., Cody, A. M., et al. 2018, AJ, 155, 196
Ricci, L., Testi, L., Natta, A., & Brooks, K. J. 2010, A&A, 521, A66
Rieke, G. H., & Lebofsky, M. J. 1985, ApJ, 288, 618
Ryabchikova, T., Piskunov, N., Kurucz, R. L., et al. 2015, PhyS, 90, 054005
Ségransan, D., Kervella, P., Forveille, T., & Queloz, D. 2003, A&A, 397, L5
Serna, J., Hernandez, J., Kounkel, M., et al. 2021, ApJ, 923, 177
Simon, M., Ghez, A. M., Leinert, C., et al. 1995, ApJ, 443, 625
Simon, M., Guilloteau, S., Beck, T. L., et al. 2019, ApJ, 884, 42
Simon, M., Schaefer, G. H., Prato, L., et al. 2013, ApJ, 773, 28
Sokal, K. R., Deen, C. P., Mace, G. N., et al. 2018, ApJ, 853, 120
Sokal, K. R., Johns-Krull, C. M., Mace, G. N., et al. 2020, ApJ, 888, 116
Torres, C. A. O., Quast, G. R., da Silva, L., et al. 2006, A&A, 460, 695
Wang, W., Gully-Santiago, M., Deen, C., Mar, D. J., & Jaffe, D. T. 2010, Proc. SPIE, 7739, 77394L
Wilking, B. A., Lada, C. J., & Young, E. T. 1989, ApJ, 340, 823
Wilking, B. A., Meyer, M. R., Robinson, J. G., & Greene, T. P. 2005, AJ, 130, 1733
Wright, J. T., & Eastman, J. D. 2014, PASP, 126, 838
Yang, H., Johns-Krull, C. M., & Valenti, J. A. 2005, ApJ, 635, 466
Yuk, I.-S., Jaffe, D. T., Barnes, S., et al. 2010, Proc. SPIE, 7735, 77351M